

Scaling Capability in Token Space: An Analysis of Large Vision Language Model

Tenghui Li

TENGHUI.LI@RIKEN.JP

*School of Automation, Guangdong University of Technology
Guangzhou 510006, China*

*Tensor Learning Team, RIKEN Center for Advanced Intelligence Project
Tokyo 103-0027, Japan*

Guoxu Zhou

GX.ZHOU@GDUT.EDU.CN

*School of Automation, Guangdong University of Technology
Guangzhou 510006, China*

Xuyang Zhao

XUYANG.ZHAO@RIKEN.JP

*Advanced Data Science Project, RIKEN Information R&D and Strategy Headquarters
Yokohama 230-0045, Japan*

*Department of Artificial Intelligence Medicine, Graduate School of Medicine, Chiba University
Chiba 260-0856, Japan*

Qibin Zhao

QIBIN.ZHAO@RIKEN.JP

*Tensor Learning Team, RIKEN Center for Advanced Intelligence Project
Tokyo 103-0027, Japan*

*School of Automation, Guangdong University of Technology
Guangzhou 510006, China*

Abstract

The scaling capability has been widely validated in neural language models with respect to the number of parameters and the size of training data. One important question is that does the scaling capability also exists similarly with respect to the number of vision tokens in large vision language Model? This study fills the gap by investigating the relationship between the number of vision tokens and the performance on vision-language models. Our theoretical analysis and empirical evaluations demonstrate that the model exhibits scalable performance $S(N_l)$ with respect to the number of vision tokens N_l , characterized by the relationship $S(N_l) \approx (c/N_l)^\alpha$. Furthermore, we also investigate the impact of a fusion mechanism that integrates the user's question with vision tokens. The results reveal two key findings. First, the scaling capability remains intact with the incorporation of the fusion mechanism. Second, the fusion mechanism enhances model performance, particularly when the user's question is task-specific and relevant. The analysis, conducted on fifteen diverse benchmarks spanning a broad range of tasks and domains, validates the effectiveness of the proposed approach.

Keywords: large language model, large vision language model, scaling capability in token space, vision-text fusion

1 Introduction

Large language models (LLMs) based on transformer architectures have demonstrated remarkable proficiency across a broad spectrum of tasks, including text generation, translation, and question-answering (Brown et al., 2020; OpenAI, 2023; Touvron et al., 2023b;

Dubey et al., 2024). One of the core components of these models is their token-based design, which involves converting text into discrete tokens for efficient processing and generation.

The token-based structure can be seamlessly adapted to other modalities through the specifically designed tokenization strategies, such as vision (Alayrac et al., 2022; Liu et al., 2023a; Bai et al., 2023b; Chen et al., 2024b; Lu et al., 2024; Hu et al., 2024; Li et al., 2023b; Dong et al., 2024), audio (Gong et al., 2024; Ghosh et al., 2024), and video (Hong et al., 2024; Zhang et al., 2023), as well as other modalities. This adaptability highlights the potential of large transformer models as versatile, multimodal systems, capable of seamlessly integrating and analyzing diverse data types in a uniform framework.

While multimodal transformer models offer impressive capabilities, a significant challenge emerges when adapting the token-based structure to high-dimensional data, such as images or videos. The tokenization of visual data frequently yields a considerable large number of tokens, reflecting the extensive and intricate information presentation within each image or frame. The resulting abundance of vision tokens can lead to increased computational costs and memory requirements, which can hinder the scalability and efficiency of these models in practical applications. For instance, in the process of image tokenization, the number of vision tokens generated during this process is primarily determined by two factors, the resolution of the input image and the tokenization strategy employed by the vision encoder. In CLIP ViT-L/14, a vision transformer model, generates 256 tokens from an image with a resolution of (224, 224), while the larger CLIP ViT-H/14 produces 576 tokens from an image with a resolution of (336, 336) (Radford et al., 2021).

Some recent vision-language models, such as InternLM-XComposer2-4KHD (Dong et al., 2024) and Phi-3 Vision (Abdin et al., 2024), have explored tokenization strategies to manage high-resolution inputs effectively. For example, in the case of a 4K image, these models employ a hybrid approach, combining one global image representation with multiple local image views. This strategy can result in a token count as high as 2377, comprising the global image token and tokens from 16 local image views, which enables the model to effectively capture both global and detailed spatial and contextual information. While the high resolution images preserve detailed spatial and contextual information, it also introduces significant computational demands due to the large amount of tokens. In contrast, other recent models adopt an opposite strategy, whereby the number of vision tokens is reduced in order to prioritize computational efficiency while retaining sufficient visual information for subsequent tasks. For example, the Q-Former architecture, employed in models such as BLIP-2 (Li et al., 2023b), reduces the number of vision tokens to a fixed count of 32. The Q-Former focuses on a small fixed collection of learnable query embeddings that dynamically capturing the most pertinent visual information. This fixed-token approach significantly reduces the computational burden, making the model more computation and memory efficient, while still maintaining a reasonable level of performance.

Since all visual information are provided by the vision tokens, both the quantity and quality of vision tokens will make a significant impact on the performance of the model. An excessive number of vision tokens can facilitate the preservation of intricate details and contextual information, yet simultaneously give rise to considerable computational and memory cost. Conversely, reducing the number of vision tokens can enhance efficiency but may result in losing critical information, thereby negatively impacting the model’s

performance. This contrast between efficiency and performance is a critical factor that needs to be carefully considered.

In this study, we aim to systematically investigate the relationship between the number of vision tokens and the performance of vision-language models. Additionally, we explore the hypothesis that fusing the user’s question into the vision token representation may lead to a measurable improvement in model performance. The key contributions and findings of this study are summarized as follows:

- We present both theoretical and experimental insights into the relationship between the number of vision tokens N_l and model performance $S(N_l)$. Our observations reveal that, in the majority of cases, the performance of the model exhibits a scaling behavior, $S(N_l) \approx (c/N_l)^\alpha$, where α shows the rate of performance changes, and c is a scalar related to the task.
- The impact of fusing the user’s question into the vision token representation is also investigated. The inclusion or exclusion of the user’s question into the vision token representation does not significantly alter the scaling behavior.
- Moreover, in most scenarios, fusing the question into the vision token representation enhances model performance, when the question is task-specific and relevant.

The rest of the paper is organized as follows: In Section 2, we provide an overview of the background and review related works relevant to this study. Section 3 presents the theoretical observations and experimental results on the impact of the number of tokens via the assumption with branch. In Section 4, we describe the main architecture and the proposed method in detail. Section 5 covers the experimental setup, results, and related analyses to validate our approach. Finally, we conclude the paper and discuss potential future research directions in Section 6.

2 Background and Related Works

2.1 Background

The majority of vision-language models are primarily driven by the advancement of two fundamental components: the large language model and the vision encoder. Based on the training strategy, vision-language models can be broadly categorized into two paradigms: natively multimodal models and hybrid models combining independently pretrained components. Natively multimodal models, such as Fuyu-8B (Bavishi et al., 2023), are jointly pretrained on vision and language tasks, enabling end-to-end learning and achieving seamless cross-modal alignment. Nevertheless, training from scratch for the large model is an extremely computationally expensive process, which presents significant challenges for researchers and practitioners with limited resources. Hybrid models, in contrast, integrate independently pretrained vision and language components into a unified framework. After integration, the unified model is fine-tuned on joint vision-language data to achieve cross-modal alignment and optimize performance. This two-stage approach reduces the computational burden of joint pretraining while enabling the reuse of state-of-the-art models on each modality. Additionally, it allows for greater modularity and flexibility, making

it easier to adapt and scale to diverse applications. Given their greater practicality and efficiency, hybrid models are more widely accepted in the field of vision-language tasks.

Pretrained Large Language Models on Text: Pretrained large language models (LLMs) have significantly advanced the field of natural language processing, enabling state-of-the-art performance on a wide range of tasks. There are several popular large language models, including GPT-4 (OpenAI, 2023), Claude (Anthropic, 2024), LLaMA (Touvron et al., 2023a,b) and its variants (Chiang et al., 2023; Taori et al., 2023), Qwen (Bai et al., 2023a), GLM (Zeng et al., 2024), and so on. These models are typically trained on large-scale text corpora and have been shown to achieve remarkable performance on various NLP tasks, such as text generation, question answering, and summarization.

Pretrained Vision Encoders: CLIP (Radford et al., 2021) is one of the foundational models in vision-language learning, designed to learn joint representations of images and text using contrastive learning. CLIP consists of separate image and text encoders, where images and text are mapped into a shared embedding space. The similarity between image-text pairs is measured in this space using a contrastive loss function. CLIP’s primary contribution lies in its ability to learn robust multimodal representations from vast amounts of publicly available image-text data. SigLIP (Zhai et al., 2023) is another image-text pre-train model, which replaces the softmax-based contrastive loss with a sigmoid loss function, enabling better scalability with smaller batch sizes and reduced computational cost.

2.2 Related Works

Pretrained large language models and vision encoders offer a solid foundation for addressing multimodal tasks. There are several strategies for integrating vision information into language models, including modifying the language model structure with adapter modules or simply treating vision tokens as instructions and concatenating them with text tokens.

Inserting Adapter Modules: By incorporating additional adapter modules into the main architecture of the language model, visual features can be seamlessly integrated alongside textual features. These adapters act as intermediary layers, facilitating the interaction between the two modalities by learning specialized transformations, allowing the model to effectively process and align multimodal information. For instance, Flamingo(Alayrac et al., 2022) applies cross-attention mechanisms between vision and language tokens, enabling it to handle open-ended tasks such as visual question answering and captioning. Similarly, CogVLM(Wang et al., 2023) incorporates a vision expert module comprising the attention and the MLP in each layer of the language model. While inserting adapter modules can achieve deeper cross-modality alignment, it comes at the cost of increased computational complexity.

Concatenating Vision Tokens: A straightforward yet efficient strategy for integrating vision and language information is to concatenate the vision tokens with the text tokens. This approach leverages the architecture of the language model to process the vision tokens in the same way as text tokens, allowing the model to bridge both modalities through its internal mechanisms without requiring additional architectural modifications. For example, LLAVA (Liu et al., 2023a), and MiniGPT-4 (Zhu et al., 2024) integrate vision tokens into the input sequence of the language model by concatenating them with text tokens. The combined token sequence is then processed by the language model, allowing the vision to-

kens to guide the language generation process. InternLM-XComposer2-4KHD (Dong et al., 2024) and Microsoft Phi-3 Vision (Abdin et al., 2024) provide enhance vision tokens by high resolution images with the global image and its local image slices. Nevertheless, this approach may require larger amount of vision tokens, which can lead to increased training and inference costs. BLIP (Li et al., 2022, 2023b) introduces lightweight query transformer (Q-Former) to provide a shorter but richer representation of the vision tokens. The Q-Former apply cross-attention between queries, some learnable placeholder tokens, and the vision tokens from the vision encoder. With this approach, less vision tokens are provided to the language model, which can lead to more efficient training while still retaining rich representations. The key advantage of the concatenation-based method is its simplicity and flexibility. It avoids complex cross-modal interaction layers, making it easier to be applied on existing vision and language models and take advantage of pretrained language models without major changes. Nevertheless, aligning vision token with text tokens could be challenging because these two set of tokens are pretrained independently. Additionally, careful design and training are required to ensure that the alignment is effective, and the vision tokens can be effectively utilized by the language model.

The research conducted by (Laurençon et al., 2024) provides a comprehensive analysis of various factors influencing the performance of vision-language large models. Key considerations include the choice of pretrained large language backbone, architectural decisions such as the adoption of autoregressive or cross-attention mechanisms, and the impact of the number of vision tokens. Different from this, our study delves further into the specific influence of the number of vision tokens, providing a detailed examination of how this parameter affects the model’s overall performance on various tasks.

Scaling Law: The scaling law (Kaplan et al., 2020), introduced empirical scaling laws that describe how the performance of neural language models, specifically the cross-entropy loss L , scales with model size N and dataset size D . The relationship is given by:

$$L(N, D) = \left[\left(\frac{N_c}{N} \right)^{\frac{\alpha_N}{\alpha_D}} + \frac{D_c}{D} \right]^{\alpha_D},$$

where N_c and D_c are constants, and α_N and α_D are empirically determined scaling exponents. This formulation indicates that both increasing the number of model parameters and expanding the dataset size lead to improvements in model performance, following a power-law relationship.

The study conducted by (Liu et al., 2024) examined a similar scaling behavior within the context space of a physical system. In contrast, our research adopts a different perspective, offering a more general framework with fewer assumptions. Additionally, our work extends these observations to the domain of vision-language models, providing a broader applicability.

2.3 Insight of Vision Token Reduction

It is crucial to investigate the feasibility of reducing the number of vision tokens while maintaining the quality of the vision-language model. Such approach could help to reduce the computational cost and storage requirements of the model, making it more practical for deployment in resource-constrained environments.

According to information theory, there are two fundamental principles on effective data reduction. The first is identifying and eliminating redundancy, which involves compressing data by removing repetitive or predictable patterns without losing essential information. The second is selective information retention, which focuses on discarding less important data elements, guided by task requirements or contextual relevance, to achieve compact and efficient representations.

These principles are directly applicable in the context of vision tokens. Vision tokens are derived from images, which often exhibit inherent redundancies, such as repetitive patterns or local similarities. Consequently, the vision tokens themselves preserve this redundancy, making them amenable to compression techniques that exploit these patterns. Additionally, in tasks like visual question answering, the text question from user may provide critical guidance for identifying the most relevant regions of the image. By aligning vision tokens with the textual query, it becomes possible to retain only the most pertinent tokens, effectively discarding irrelevant or less important information without compromising the performances.

Based on the discussion, the reduction of vision tokens in vision-language models is a promising approach to improve efficiency and scalability.

3 Branch by Appending Tokens

In this section, we will introduce a branching mechanism generated by appending tokens and its theoretical discussion. Briefly speaking, the upper bound of the distance between two branches is $\mathcal{O}\left(\sqrt{\psi(N)N^2 + (1 - \psi(N))N}\right)$, where N is the sequence length and $\psi(N)$ indicate the behavior of a specific sequence model.

3.1 Preliminaries

Vision-language models operate on two primary types of inputs: text tokens and vision tokens. Considering concatenation-based methods, the formatted input sequence of these two sets of tokens can be represented as:

$$[T_1, \dots, T_k, |M_{k+1}, M_{k+2}, \dots, M_{k+n}|, T_{k+n+1}, T_{k+n+2}, \dots],$$

where T_1, T_2, \dots, T_k are text tokens, $M_{k+1}, M_{k+2}, \dots, M_{k+n}$ are vision tokens, and T_{k+n+1}, \dots indicate remaining text tokens. To establish the conceptual foundation of the problem, we consider an idealized model of sequence generation. This model assumes the following settings:

- **Valid Tokens:** Vision tokens are well-aligned with text tokens and can be treated as newly introduced tokens in the sequence.
- **Text Prefix:** The initial portion of the sequence consists of a fixed prefix of text tokens.
- **Incremental Addition:** New tokens from different sources are appended to the same prefixed text tokens incrementally, one token at a time.

Given these assumptions, we introduce a branching mechanism that reflects the model’s ability to dynamically generate new sequence of tokens based on the inserted additional tokens. Let the initial sequence of tokens be represented as $\mathbf{a}_1, \mathbf{a}_2, \dots$. At a specific time step t , the sequence is branched by appending new tokens $\mathbf{b}_t, \mathbf{b}_{t+1}, \dots$

$$\mathbf{a}_1, \mathbf{a}_2, \dots, \mathbf{a}_{t-1} \begin{cases} \rightarrow \mathbf{a}_t, \mathbf{a}_{t+1}, \dots \\ \rightarrow \mathbf{b}_t, \mathbf{b}_{t+1}, \dots \end{cases}$$

At time step t , the sequence is diverged into two distinct branches. The original sequence continues with tokens $\mathbf{a}_t, \mathbf{a}_{t+1}, \dots$, while the new branch is formed by additional tokens $\mathbf{b}_t, \mathbf{b}_{t+1}, \dots$. If only few tokens are added to the new branch at time step t , it is possible that the language model may not have enough information to make distinct predictions for this new branch. As a result, the predictions generated for the new branch may closely resemble those of the original branch, leading to minimal divergence between the two sequences. In contrast, when a larger number of tokens are introduced, providing more comprehensive information, the model is better equipped to generate predictions that are significantly different from those of the original branch. As a result, new branch is created.

This idealized model serves as a simplified representation of concatenation-based vision-language models. In this context, consider the system prompt and user query as the initial sequence $\mathbf{a}_1, \mathbf{a}_2, \dots, \mathbf{a}_{t-1}$. At time step t , a vision token is introduced into the sequence, initiating a new branch. As more vision tokens are added to this branch, it gradually becomes more distinct from the original sequence. Eventually, after a certain threshold is reached, the divergence between the two branches becomes significant. At this point, the language model can generate a sequence that is closely aligned with the content of the image, reflecting a strong integration of visual and textual information.

A brief overview of this idealized model is provided in Figure 1. In this figure, the blue line represents the initial sequence. At a specific time step, new branches are created by appending additional tokens to the sequence. After a certain threshold, the divergences between the branches become significant, and the model can generate sequences that are closely aligned with the content of the additional tokens.

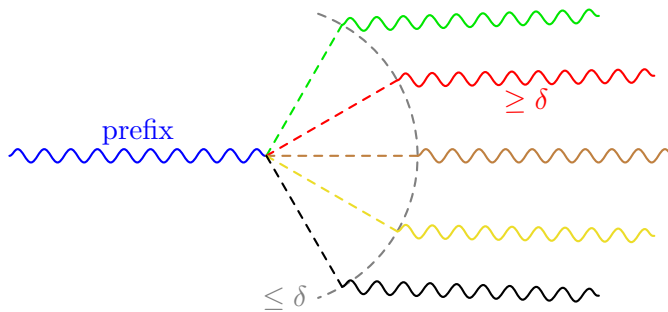


Figure 1: A simplified representation of the idealized model.

In light of this assumption, determining the threshold value is crucial for understanding the dynamics of sequence branching in the idealized model. The threshold represents the point at which the addition of vision tokens leads to significant divergence between the

original sequence and the newly branched sequence. By establishing this threshold, it is possible to estimate the minimum number of vision tokens required to generate a response that is highly relevant to the visual input.

3.2 Branches Under Mapping

To assess the threshold value for significant sequence divergence, it is first necessary to define a measure of distance between two branches. In this subsection, a mapping mechanism is introduced to help estimate the distance between two branches.

Consider two sequences of tokens, $[\hat{\mathbf{a}}_1, \hat{\mathbf{a}}_2, \dots]$ and $[\hat{\mathbf{b}}_1, \hat{\mathbf{b}}_2, \dots]$. We assume the existence of a transformation mapping $g_i(\cdot)$ on each token, such that $g_i(\hat{\mathbf{a}}_i) = \mathbf{a}_i$ and $g_i(\hat{\mathbf{b}}_i) = \mathbf{b}_i$. The transformation mapping $g_i(\cdot)$ should reflect the behavior of the model. Specifically, we consider the mapping $g_i(\cdot)$ as,

$$g_i(\hat{\mathbf{a}}_i) := \text{SequenceModel}(\hat{\mathbf{a}}_1, \dots, \hat{\mathbf{a}}_i),$$

where the sequence model takes all preceding tokens as input to generate the output token. For a more specific case, we consider the sequence model as a decoder-only transformer model. The mapping $g_i(\cdot)$ could be considered as

$$g_i(\hat{\mathbf{a}}_i) = \text{LLM}(\hat{\mathbf{a}}_1, \dots, \hat{\mathbf{a}}_i)[-1],$$

where LLM represent the decoder-only transformer model without the final linear layer, and $\text{LLM}(\dots)[-1]$ denotes the last item of output sequence.

The distance between the two branches is then computed based on the mapped tokens, \mathbf{a}_i and \mathbf{b}_i , providing a quantitative measure of how far apart the two sequences have diverged over time.

To further understand the divergence, consider the mapped tokens at each time step i as points in a high-dimensional space, where the sequence progression can be likened to a random walk. Suppose all branches begin at the same initial point, represented as the origin in this space. For instance, in the sequence $[\mathbf{a}_1, \dots, \mathbf{a}_N]$, the branch starts at the origin at time step 0. At time step 1, the branch moves from the origin to the point \mathbf{a}_1 . This process continues step by step, with the branch moving from its current position towards \mathbf{a}_i at each subsequent time step i . The movement of the branch through this high-dimensional space forms a relatively random path. The final destination of the branch after N steps being represented by the cumulative sum $\sum_{i=1}^N \mathbf{a}_i$. The difference between the two branches after N steps can be expressed as,

$$\left(\sum_{i=1}^N \mathbf{a}_i \right) - \left(\sum_{i=1}^N \mathbf{b}_i \right) = \sum_{i=1}^N \left(g_i(\hat{\mathbf{a}}_i) - g_i(\hat{\mathbf{b}}_i) \right) := \sum_{i=1}^N \Delta \mathbf{g}_i, \quad (1)$$

where $\Delta \mathbf{g}_i$ denotes the difference $g_i(\hat{\mathbf{a}}_i) - g_i(\hat{\mathbf{b}}_i)$ for each time step i . To gain a more nuanced understanding of the distance between the two branches, a weight vector \mathbf{w} with $\|\mathbf{w}\|_F = 1$ is introduced, where $\|\cdot\|_F$ denotes the Frobenius norm. The weighted distance between the branches can then be analyzed via the expectation,

$$\mathbb{E} \left(\mathbf{w}^T \left(\sum_{i=1}^N \left(g_i(\hat{\mathbf{a}}_i) - g_i(\hat{\mathbf{b}}_i) \right) \right) \right), \quad (2)$$

where, \mathbf{w}^T represents the transpose of the weight vector \mathbf{w} , and \mathbb{E} denotes the expectation operator.

Since both sequences of tokens $\widehat{\mathbf{a}}_i$ and $\widehat{\mathbf{b}}_i$ are drawn from the same space, they share the same statistical properties. Moreover, the transformation mapping $g_i(\cdot)$ is applied uniformly to both sequences. As a result, the mapped tokens $g_i(\widehat{\mathbf{a}}_i)$ and $g_i(\widehat{\mathbf{b}}_i)$ also share the same distribution, indicating that $\mathbb{E}(g_i(\widehat{\mathbf{a}}_i)) = \mathbb{E}(g_i(\widehat{\mathbf{b}}_i))$. Given that the transformation is consistent across both sequences, the expected value of the difference between the mapped tokens should be zero for any $i \in [1, N]$,

$$\mathbb{E}(g_i(\widehat{\mathbf{a}}_i) - g_i(\widehat{\mathbf{b}}_i)) = \mathbb{E}(g_i(\widehat{\mathbf{a}}_i)) - \mathbb{E}(g_i(\widehat{\mathbf{b}}_i)) = 0. \quad (3)$$

For a sequence model, the output token at position i is computed based on all preceding tokens from position 1 to i . Consequently, $g_i(\widehat{\mathbf{a}}_i)$ is not independent of $g_j(\widehat{\mathbf{a}}_j)$ for $1 \leq j < i$. Therefore, it is not reasonable to assume that the tokens in a sequence are independent of each other. Instead, the difference between mapped tokens cannot be simply computed by assuming independence, and their relationships must be taken into consideration.

When processing branching sequences that share the same initial sequence, the tokens in the two branches are likely to exhibit a degree of commonality, particularly if the length of the branching sequence is relatively short. In such cases, the information from the initial sequence can be effectively carried over to the branching sequence, leading to greater similarity between the tokens in the two branches. Consequently, $g_i(\widehat{\mathbf{a}}_i)$ and $g_i(\widehat{\mathbf{b}}_i)$ are less likely to be independent of each other, especially when i is small. There are two main reasons for this similarity. Firstly, they shared the same initial context, ensuring that the tokens generated in the branches are influenced by the same underlying information, contributing to their similarity. Secondly, the tokens in both branches are generated by the same sequence model, which applies its knowledge and understanding of the context uniformly across both branches. This consistency in the model's processing further aligns the tokens in the branches, reinforcing their similarity. Therefore, when the branching sequences are short, the tokens in the two branches are less likely to be independent of each other, as they share a common context and are generated by the same sequence model. This kind of dependency should be taken into account when analyzing the divergence between branches and estimating the threshold value.

Due to the inherent dependency among tokens in a sequence model, the difference $\Delta \mathbf{g}_i = g_i(\widehat{\mathbf{a}}_i) - g_i(\widehat{\mathbf{b}}_i)$ is also likely to be dependent for $1 \leq j < i$. In the following analysis, we will explore the expectation of these differences while considering their interdependencies. The expectation in Equation (2) can be further analyzed as follows,

$$\begin{aligned} \mathbb{E} \left(\mathbf{w}^T \left(\sum_{i=1}^N \Delta \mathbf{g}_i \right) \right) &\leq \mathbb{E} \left(\left\| \sum_{i=1}^N \Delta \mathbf{g}_i \right\|_F \right) \\ &\leq \left(\mathbb{E} \left(\left\| \sum_{i=1}^N \Delta \mathbf{g}_i \right\|_F^2 \right) \right)^{1/2}. \end{aligned} \quad (4)$$

Expanding the expectation in the right-hand side of Inequality (4), and splitting the terms into two parts, we have

$$\mathbb{E} \left(\left\| \sum_{i=1}^N \Delta \mathbf{g}_i \right\|_F^2 \right) = \sum_{i=1}^N \mathbb{E} (\|\Delta \mathbf{g}_i\|_F^2) + \sum_{i,j=1, i \neq j}^N \mathbb{E} ((\Delta \mathbf{g}_i)^T \Delta \mathbf{g}_j). \quad (5)$$

If $\Delta \mathbf{g}_i$ and $\Delta \mathbf{g}_j$ are independent for $i \neq j$, then the expectation of the cross terms will approx to zero, $\mathbb{E} ((\Delta \mathbf{g}_i)^T \Delta \mathbf{g}_j) = 0$. This implies that the second part of the right-hand side of Inequality (5) is zero, and the upper bound is determined by the first part,

$$\sum_{i=1}^N \mathbb{E} (\|\Delta \mathbf{g}_i\|_F^2) \leq N \max_{i \in [1, N]} \|\Delta \mathbf{g}_i\|_F^2. \quad (6)$$

Nevertheless, this assumption is not satisfied in the case of the large language model, since a token is always related to all previous tokens. Consequently, the cross term is not zero in general. To address this issue, we attempt to describe the cross terms via a probability distribution.

Let Θ_{ij} be the angle between $\Delta \mathbf{g}_i$ and $\Delta \mathbf{g}_j$. Based on the property of inner product, we have

$$\begin{aligned} \sum_{i,j=1, i \neq j}^N \mathbb{E} ((\Delta \mathbf{g}_i)^T \Delta \mathbf{g}_j) &= \sum_{i,j=1, i \neq j}^N \mathbb{E} (\|\Delta \mathbf{g}_i\|_F \|\Delta \mathbf{g}_j\|_F \cos \Theta_{ij}) \\ &\leq \sum_{i,j=1, i \neq j}^N \mathbb{E} (\cos \Theta_{ij}) \max_{k \in [1, N]} \|\Delta \mathbf{g}_k\|_F^2. \end{aligned}$$

In order to further bound the cross terms, an important assumption is introduced as Assumption 1.

Assumption 1 (Dependency via Probability Distribution) *There is a probability distribution on $\cos \Theta_{ij}$ with respect to N , and $\mathbb{E}_{i,j \in [1, N], i \neq j} (\cos \Theta_{ij}) \leq 1$. Let the probability be designated as $P_N\{\cos \Theta_{ij}\}$, we have*

$$\psi(N) = \sup \mathbb{E}_{i,j \in [1, N], i \neq j} (\cos \Theta_{ij}) = \sup \int_{-\infty}^{+\infty} (\cos \Theta_{ij}) P_N\{\cos \Theta_{ij}\} d\Theta_{ij}, \quad (7)$$

where \sup indicate the supremum of the set.

In light of assumption 1, the sum of expectations on the cross terms can be further bounded as

$$\sum_{i,j=1, i \neq j}^N \mathbb{E} ((\Delta \mathbf{g}_i)^T \Delta \mathbf{g}_j) \leq (N^2 - N) \psi(N) \max_{i \in [1, N]} \|\Delta \mathbf{g}_i\|_F^2. \quad (8)$$

Combining the two parts from inequality (6) and (8), we have

$$\begin{aligned} \mathbb{E} \left(\left\| \sum_{i=1}^N \Delta \mathbf{g}_i \right\|_F^2 \right) &\leq N \max_{i \in [1, N]} \|\Delta \mathbf{g}_i\|_F^2 + (N^2 - N) \psi(N) \max_{i \in [1, N]} \|\Delta \mathbf{g}_i\|_F^2 \\ &= (\psi(N) N^2 + (1 - \psi(N)) N) \max_{i \in [1, N]} \|\Delta \mathbf{g}_i\|_F^2. \end{aligned} \quad (9)$$

Plugging the result in inequality (9) into inequality (4), we have

$$\begin{aligned} \mathbb{E} \left(\mathbf{w}^T \left(\sum_{i=1}^N \Delta \mathbf{g}_i \right) \right) &\leq \sqrt{\psi(N)N^2 + (1 - \psi(N))N} \max_{i \in [1, N]} \|\Delta \mathbf{g}_i\|_F \\ &= \mathcal{O} \left(\sqrt{\psi(N)N^2 + (1 - \psi(N))N} \right). \end{aligned} \quad (10)$$

3.3 Properties of The Bound

The inequality (10) provides a general bound for the expectation of the distance between two sequences of tokens. This bound is influenced by two key factors: the length of the branch sequence N and the function $\psi(N)$, which represents the expectation of the cosine of the angle between two tokens in the sequence. To quantify the impact of these two factors, we define the function $f(N) = \sqrt{\psi(N)N^2 + (1 - \psi(N))N}$.

Let us first assume that $\psi(N) = \psi$ is a constant for all N , $f(N) = \sqrt{\psi N^2 + (1 - \psi)N}$. The function $f(N)$ exhibits two extreme cases depending on the value of N . When N is small, the term $(1 - \psi)N$ becomes more significant compared to ψN^2 , leading to an approximation of $f(N) \approx \mathcal{O}(\sqrt{N})$. Conversely, when N is large, the term ψN^2 dominates over $(1 - \psi)N$, resulting in an approximation of $f(N) \approx \mathcal{O}(N)$. A brief overview of the function $f(N)$ under these conditions is illustrated in Figure 2.

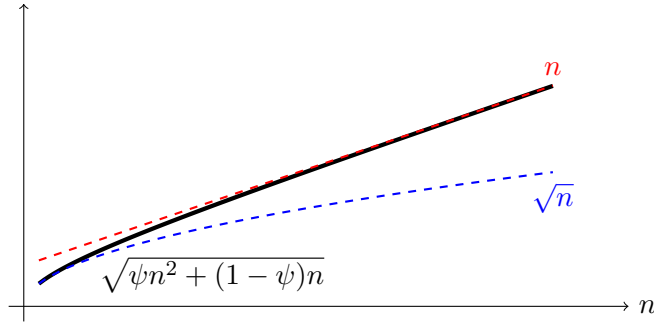


Figure 2: A brief overview of two extreme cases for function $f(n) = \sqrt{\psi n^2 + (1 - \psi)n}$.

Next, we consider the case where $\psi(N)$ is a function of N . Since $\psi(N) = \sup \mathbb{E}(\cos \Theta_{ij})$, it follows that $-1 \leq \psi(N) \leq 1$ for all $N \geq 1$. The maximum value of $\psi(N)$ is attained when $\cos \Theta_{ij} = 1$ for all pairs, while the minimum value is reached under the condition that all $\cos \Theta_{ij} = -1$. In the case where $\psi(N) = 0$, it indicates that the expected cosine similarity between different pairs is zero, suggesting no correlation between the pairs. For $N = 1$, the function $f(N)$ simplifies to $f(1) = 1$. This is because with a single token in the sequence, the distance between the two sequences is trivially zero, leading to a constant value of 1 in this special case. When $N > 1$, to ensure the square root is computable, requires that $\psi(N)N^2 + (1 - \psi(N))N \geq 0$. This implies that $\psi(N) \geq -1/(N - 1)$. As N increases, $-1/(N - 1)$ will approach to zero. To ensure that the square root function is computable for any given value of N , it is reasonable to consider the value domain of the function $\psi(N)$ to the interval $[0, 1]$.

In the context of sequence models, particularly large language models, the function $\psi(N)$ is expected to exhibit specific characteristics based on the length of the branching sequence. When the new branch is short, the predicted tokens from the model are more likely to rely on the shared prefix tokens. In such cases, the cosine similarity between the two sequences is expected to be high, leading to a large value of $\psi(N)$. This high similarity reflects that the branch is still closely aligned with the original sequence, sharing significant contextual information. Conversely, if the new branch is long, the model has greater flexibility to generate diverse outputs based on the extended sequence. As a result, the dependency on the shared prefix diminishes, and the cosine similarity between the sequences is likely to be lower. This results in a smaller value of $\psi(N)$, indicating increased divergence between the sequences as the branch grows longer.

3.4 Threshold Derivation

Based on the characteristics of the bound introduced in subsection 3.3, it is possible to derive a threshold value for sequence divergence. This threshold helps in understanding at what point the divergence between sequences becomes significant. In the following, we propose two methods to derive this threshold.

The first method for deriving the threshold involves analyzing the ratio of the bound with respect to contributions of the terms in the bound. As N increases, the bound approaches $\mathcal{O}(N)$. A ratio can be calculated as,

$$\frac{\sqrt{\psi(N)N^2 + (1 - \psi(N))N}}{\sqrt{\psi(N)N^2}} \propto \frac{1 - \psi(N)}{\psi(N)N}. \quad (11)$$

The ratio measures the relative contribution of the second term in the bound compared to the first term. To derive an appropriate threshold, set ρ to a predefined threshold value, we have $(1 - \psi(N))/(\psi(N)N) \leq \rho$. Solving for N gives,

$$N \geq \frac{1 - \psi(N)}{\psi(N)\rho}. \quad (12)$$

The second method for deriving the threshold involves a direct analysis of the function $\psi(N)$. As discussed in subsection 3.3, $\psi(N)$ is a decreasing function of N .

Initially, when the branching sequence is short, $\psi(N)$ is expected to be large, reflecting a high similarity between the sequences due to the significant overlap in their context and information. As the length of the branch sequence increases, the model has more room to diverge from the original sequence, leading to a gradual decrease in $\psi(N)$. Eventually, the divergence between the sequences becomes significant, and $\psi(N)$ stabilizes at a low value.

In order to identify a threshold, we observe the gradient $d\psi(N)/dN$. Since N is discrete, the gradient computation can be approximated by the difference,

$$\Delta\psi(N) = \psi(N + 1) - \psi(N). \quad (13)$$

The threshold can be taken via a predefined small value δ such that,

$$N = \operatorname{argmin}_n \Delta\psi(n) \geq \delta. \quad (14)$$

3.5 Empirical Estimation of The Upper Bound

In this subsection, the expectation $\mathbb{E} \left(\left\| \sum_{i=1}^N \Delta \mathbf{g}_i \right\|_F \right)$ and the function $\psi(N)$ is estimated empirically on pretrained large language models and a dataset of paired sequences. Based on the empirical estimates on them, we derive a threshold value that indicates the sequence length at which the divergence between the original and branching sequences becomes significant.

To facilitate this estimation, a dataset of paired input sequences is required. Each pair should consist of an initial sequence and a branching sequence of varying lengths. Specifically, a sequence comprises three components: a system prompt, a query, and an answer. In each pair, the system prompt and query remain identical, while the answers differ, creating positive and negative sequences. The difference $\Delta \mathbf{g}_i$ is computed specifically based on the ‘answer’ component of the positive and negative sequences. This approach allows for a focused analysis of how divergence in the answers reflects changes in the sequence and helps in deriving meaningful empirical estimates for $\psi(N)$ and the associated expectation.

In order to conduct the empirical analysis, a dataset that is well-suited to the task at hand is required. The dataset requirements are closely aligned with those used in Direct Preference Optimization (DPO) (Rafailov et al., 2023). Specifically, we utilize the dataset ‘orca-dpo-pairs’¹, which contains the necessary paired sequences to conduct this estimation.

The detailed computation process is described as follows. Firstly, the positive and negative sequences are converted to the input tokens $\hat{\mathbf{a}}_i$ and $\hat{\mathbf{b}}_i$. Secondly, the input tokens are passed through the mapping $g_i(\cdot)$. The mapping is taken as the last token on the output sequence of a large language model, excluding the last output embedding layer,

$$\begin{aligned} g_i(\hat{\mathbf{a}}_i) &= \text{LLM}(\cdots, \hat{\mathbf{a}}_t, \hat{\mathbf{a}}_{t+1}, \cdots, \hat{\mathbf{a}}_{t+i})[-1]; \\ g_i(\hat{\mathbf{b}}_i) &= \text{LLM}(\cdots, \hat{\mathbf{b}}_t, \hat{\mathbf{b}}_{t+1}, \cdots, \hat{\mathbf{b}}_{t+i})[-1]. \end{aligned}$$

Thirdly, the difference $\Delta \mathbf{g}_i = g_i(\hat{\mathbf{a}}_i) - g_i(\hat{\mathbf{b}}_i)$ is computed only on the ‘answer’ component, and N equals to the length of the ‘answer’ component. The reasoning behind this is that the ‘answer’ component is the only part of the sequence that differs between the positive and negative sequences. If the answer of the positive and negative sequences are not the same, then the longer sequence is truncated. Lastly, the empirical estimation is taken based on various amount of collected data.

Recalling Equation (2), we take the same weight of each element of the token, picking \mathbf{w} with all entries equal to $1/\|\mathbf{w}\|_F$, the expectation could be estimated as,

$$\mathbb{E} \left(\left\| \sum_{i=1}^N \Delta \mathbf{g}_i \right\|_F \right). \quad (15)$$

By Equation (7), the function $\psi(N)$ can be estimated by the empirical estimation of $\mathbb{E}(\Theta_{ij})$,

$$\begin{aligned} \psi(N) &\Leftarrow \mathbb{E}_{i,j \in [1,N], i \neq j} (\cos \Theta_{ij}) \\ &\Leftarrow \mathbb{E} \left(\frac{1}{N-1} \sum_{i,j=1, i < j}^N \frac{(\Delta \mathbf{g}_i)^T (\Delta \mathbf{g}_j)}{\|\Delta \mathbf{g}_i\|_F \|\Delta \mathbf{g}_j\|_F} \right). \end{aligned} \quad (16)$$

1. https://huggingface.co/datasets/Intel/orca_dpo_pairs

Recall Inequality (10), the theoretical analysis shows that the expectation is bounded by,

$$\lambda\sqrt{\psi(N)N^2 + (1 - \psi(N))N}, \quad (17)$$

where the hyperparameter λ is taken as

$$\lambda = \operatorname{argmin}_{\lambda} \left(\mathbb{E} \left(\left\| \sum_{i=1}^N \Delta \mathbf{g}_i \right\|_F \right) - \lambda\sqrt{\psi(N)N^2 + (1 - \psi(N))N} \right)^2. \quad (18)$$

The estimated $\psi(N)$ for various models is shown in Figure 3a. From the figure, we observe that the estimated function $\psi(N)$ aligns closely with the theoretical analysis. Specifically, $\psi(N)$ exhibits a high value when the length of the sequence is small, indicating a high similarity between the sequences. As the length of the sequence increases, $\psi(N)$ decreases, eventually approaching a relatively stable value.

An example of the estimation performed on the pretrained large language model ‘Llama 2 7B’ is shown in Figure 3b. From this figure, we observe that the empirical estimation of the expectation is in close agreement with the theoretical bound, with the hyperparameter λ set to 148.15. Additional examples can be found in Appendix A.

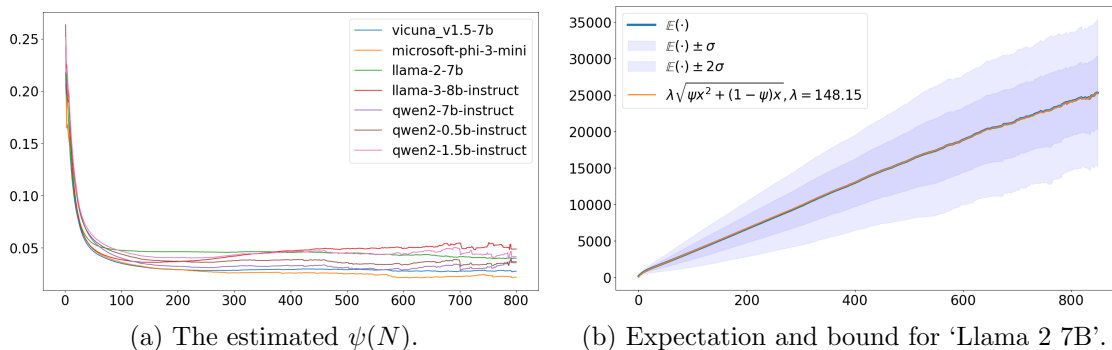


Figure 3: The estimated $\psi(N)$ and an example of the expectation with the bound.

Based on the estimated $\psi(N)$, we can determine a threshold for sequence divergence as described in subsection 3.4.

The first method involves checking the ratio of the theoretical bound with respect to the term $\mathcal{O}(N)$. The results of this method are illustrated in Figure 4a. The second method involves analyzing the gradient of $\psi(N)$ using the discrete difference, with the results shown in Figure 4b.

From Figure 4a, we observe that the ratio is relatively high when the sequence length is small, indicating a high similarity between the sequences. As the sequence length increases, the ratio decreases, eventually stabilizing at a relatively low value. For example, the dashed line in Figure 4a represents the value of $y = 0.3$, and it can be seen that when the ratio is less than 0.3, the length N is roughly 100. Figure 4b shows that the discrete difference is relatively unstable when the sequence length is short, reflecting variability in similarity. However, as the sequence length increases, the discrete difference approaches zero, indicating that the sequences have diverged significantly and the similarity between them has stabilized.

at a low level. Notably, there are some fluctuations when N is large; this instability is primarily due to the insufficient number of samples to accurately estimate the discrete difference. From the figure and its zoomed-in view, it can be observed that the discrete difference becomes relatively stable as N increase.

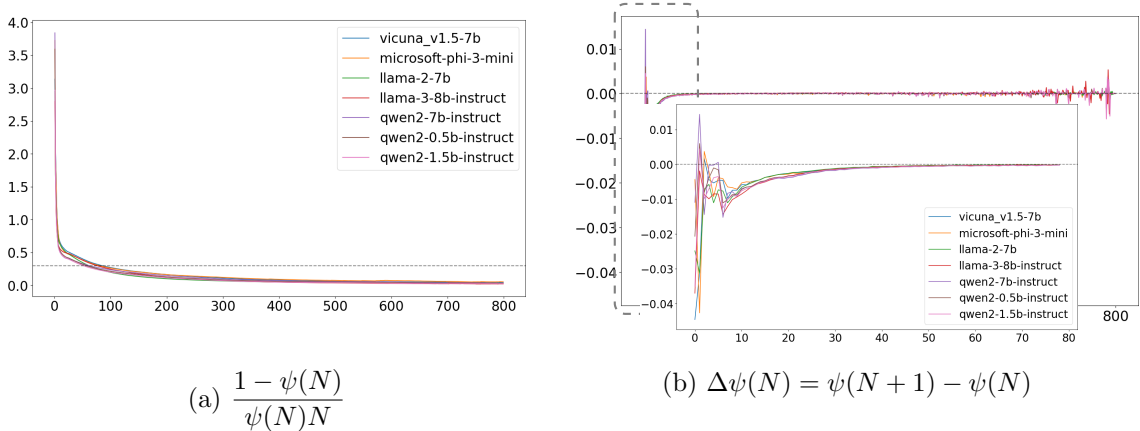


Figure 4: Threshold derivation via the ratio and the discrete difference.

4 Proposed Model

In this section, we introduce a vision-language model that leverages a concatenation-based approach on pretrained foundation models. The inputs to the large language model are formed by concatenating text tokens with vision tokens, which is widely adopted in vision-language models for its straightforward yet effective integration of multimodal information.

To enhance the integration between vision and language modalities, a fusion mechanism is designed to optimize the vision tokens before they are concatenated with the text tokens. This mechanism is designed to control the number of vision tokens while preserving the most relevant information, thereby improving the quality of the final representation.

4.1 Preliminaries

As discussed in Section 3, the expectation of distance between two branches can be expressed as a function of N , the number of newly appended tokens. With N increase, the difference between the two branches stabilizes, suggesting a convergence in behavior. In light of the preceding discussion in Subsection 2.3, and the perspective of information theory, reducing the number of vision tokens becomes feasible when redundancy exists or when effective guidance mechanisms are introduced to eliminate irrelevant information. According to the actual application, one effective source of guidance is the question provided in the user’s question. This question can serve as a pivotal mechanism to focus the model’s attention on relevant visual information while discarding unrelated content.

To leverage these insights, we propose a fusion module designed to integrate vision tokens with text tokens derived from the user’s question. By aligning visual features with linguistic

cues, the fusion module is able to filter out irrelevant information, and dynamically refine its understanding of the visual scene in the context of the question.

4.2 Main Architecture

The main architecture of the proposed model is illustrated in Figure 5. There are three primary components in the proposed model: a vision encoder, a fusion module, and a large language model backbone. Each module is designed to fulfill a specific function, ensuring the seamless integration of vision and language modalities.

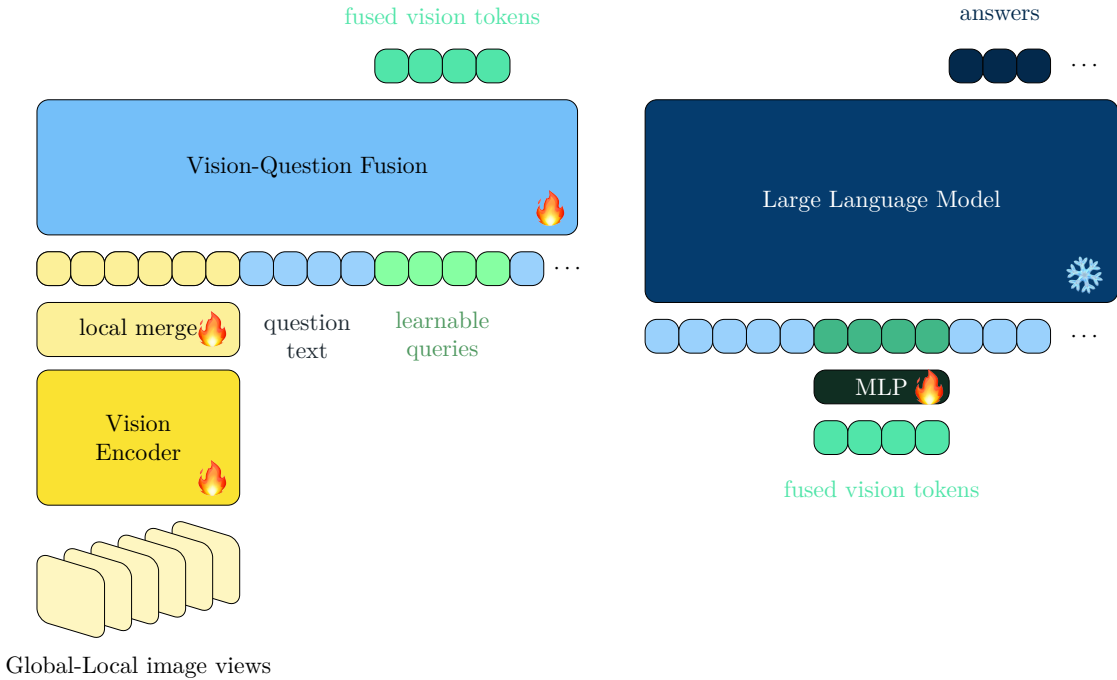


Figure 5: The architecture of the proposed model. Vision tokens are fused with question text and learnable queries before being processed by the LLM. Modules marked with ‘fire’ are updated during fine-tuning, whereas modules marked with ‘snowflake’ remain frozen.

The **vision encoder** processes input images and generates a set of vision tokens, encapsulating the visual information extracted from the input. Nevertheless, when employing CLIP ViT-H/14 (Radford et al., 2021) as the vision encoder, the resolution of input images is restricted to (336, 336). While this resolution is adequate for general tasks, it becomes a limitation for applications requiring fine-grained details, such as recognizing small objects, reading optical characters, and so on. To address this issue, we propose leveraging high resolution image crops as input to the vision encoder. High-resolution images could provide richer detail and enhance the model’s ability to capture subtle visual features that may be missed at lower resolutions.

The preprocessing of high-resolution images is inspired by the methodology employed in methods (Dong et al., 2024; Abdin et al., 2024). The input image will be transformed into two distinct categories of views: global view and local views. For the global view, the

input image is padded and zoomed to match the desired resolution, providing a holistic view of the image, preserving its overall context and structure. Conversely, for local views, the input image is padded and zoomed as necessary and then divided into smaller views, with each view having the desired resolution. This global-local view approach allows the model to focus on localized details within the image, capturing fine-grained features that may be critical for downstream tasks.

To efficiently manage the large number of vision tokens generated during the global-local view preprocessing, a local merge strategy is employed, wherein multiple vision tokens, such as four neighboring tokens, are aggregated into a single token, thereby reducing the token count by a factor of four and streamlining the subsequent processing stages. This preprocessing methodology enables the vision encoder to process high-resolution images without any adaptations required to its underlying architecture.

The **fusion module** is designed to serve two distinct requirements: firstly, to control the number of vision tokens; and secondly, to integrate vision tokens with text tokens derived from text questions.

To achieve the first requirement, the fusion module incorporates learnable queries that dynamically interact with vision tokens to distill the most relevant visual information. These learnable queries, inspired by the Q-Former (Li et al., 2023b), act as intermediaries, selectively attending to important features in the vision tokens. In contrast to the Q-Former, our fusion model also integrates with text questions, thereby aligning the token selection process with task-specific requirements. This approach ensures that the vision tokens are filtered and focused based on the context provided by the user’s question, effectively reducing the number of vision tokens while preserving task-critical features.

For the second requirement, the fusion module employs a decoder-only self-attention transformer to integrate the vision tokens with text tokens. In the cross-attention operation, the learnable queries and text tokens are positioned in the query matrix \mathbf{Q} , while the vision tokens are placed in the key-value matrices \mathbf{K} and \mathbf{V} , respectively. During the computation of attention scores, the queries in \mathbf{Q} interact exclusively with the vision tokens from \mathbf{K} and \mathbf{V} , ensuring that vision-text alignment remains the primary focus. However, interaction between different entities in \mathbf{Q} , such as two rows \mathbf{Q}_i and \mathbf{Q}_j for $i \neq j$, is also essential to capture contextual relationships within \mathbf{Q} . To enable these interactions within \mathbf{Q} , additional self-attention mechanisms are required. To maintain simplicity and efficiency, the fusion module incorporates a decoder-only self-attention transformer architecture, following the structure of Llama (Touvron et al., 2023b). Moreover, to reduce the computational complexity from self-attention, the fusion module is designed to be lightweight, with a relatively small hidden size and fewer layers. With this structure and following the causal mechanism, rich interactions between entities in visual tokens, text tokens or learnable queries can be achieved.

The third component is the **large language model** backbone, a powerful transformer architecture pretrained exclusively on huge amounts of text data. Since these large language models are trained solely on textual inputs, they are not inherently designed to process or understand visual information. To address this limitation, additional visual information is incorporated by concatenating the text tokens with the fused tokens generated by the fusion module. If needed, a projection layer is applied to ensure the fused tokens are properly aligned in shape with the text tokens.

To enable the large language model to effectively process multimodal input, it is essential to ensure proper alignment between the fused vision tokens and the text tokens. This alignment is facilitated through fine-tuning on vision-text dataset, ensuring that the LLM can accurately interpret the integrated visual information and produce coherent, context-aware responses. One of the key focuses of this research is to explore the relationship between the number of fused vision tokens and the overall performance of the model. To isolate and analyze this relationship effectively, the large language model backbone is kept frozen during fine-tuning, allowing the study to concentrate solely on the fused vision tokens, rather than being confused by changes in the LLM. Therefore, only the parameters of the fusion module, the vision encoder, and some other projection layers are updated.

4.3 Formats of Token Sequences

In this subsection, we introduce the formats of token sequences employed in the proposed architecture outlined in Subsection 4.2. Two distinct token sequence formats are introduced, each corresponding to a critical stage in the main architecture. The first format represents the input to the fusion module, while the second format pertains to the input to the large language model.

Input format to the fusion module: The input to the fusion module is constructed by concatenating three distinct types of tokens: the vision tokens, which are generated by the vision encoder and encapsulate visual features extracted from the input image; the text tokens, derived from the question text and mapped through the embedding layer; and a set of learnable queries, which are sourced from a fixed codebook and designed to facilitate selective attention within the fusion module.

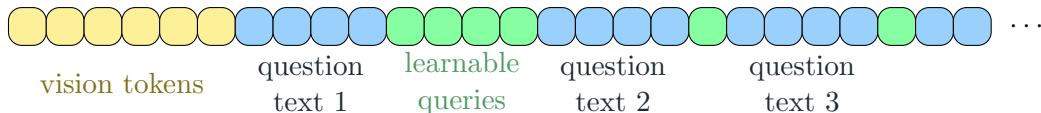


Figure 6: Example of the input token sequence to the fusion module.

An example of the input token sequence to the fusion module is illustrated in Figure 6. This format enables efficient handling of multiple inputs, facilitating processing in multiple question and multiple answer tasks. Specifically, we vary the length of the learnable queries such that the first question is followed by N_l learnable queries, while each subsequent question is followed by N_s learnable queries, where $N_s < N_l$.

This design is motivated by two key reasons. Firstly, there is common information shared across all questions, which can be encoded in the first N_l learnable queries. These queries capture shared context and general features that benefit all subsequent questions. For the remaining questions, only question-specific information needs to be encoded, allowing the use of shorter N_s learnable queries. This design efficiently balances the inclusion of shared and question-specific information while reducing redundancy. Secondly, this approach significantly reduces the total number of learnable queries, as well as the corresponding fused vision tokens. For K questions, using N_l learnable queries for all questions would result in $K \times N_l$ learnable queries. In contrast, by employing N_l learnable queries after the first question and N_s learnable queries after the remaining questions, the total is reduced to

$N_l + K \times N_s$, where $N_s < N_l$. This reduction enhances computational efficiency and scalability.

Input format to the large language model: Each large language model requires its specific input format to ensure effective processing. To incorporate the fused vision tokens into the LLM input, these tokens are positioned at the beginning of the input sequence for each question, while all other text structures remain unchanged. This arrangement ensures that the visual information is readily accessible to the model, providing a consistent context for interpreting the question-specific tokens that follow. An example of this input format is shown in Figure 6, where the lengths of the fused vision tokens follow the same pattern as the learnable queries, with the first question using N_l tokens and the remaining questions using N_s tokens.

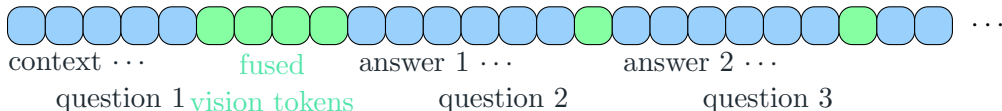


Figure 7: Example of the input token sequence to the fusion module. If needed, the fused vision token would be projected to match the shape of the LLM.

4.4 Loss Functions

Since the fusion module is newly introduced and initialized randomly, it requires careful training to effectively adapt to the task. To achieve this, we design a training strategy that incorporates complementary loss functions, each addressing specific aspects of the task. Two key loss functions are employed: the contrastive loss and the identity loss. The training pipeline involves two principal stages. Initially, preliminary training is conducted on the vision encoder, the fused model with the contrastive loss, and subsequently, fine-tuning is performed with the large language model backbone on generation loss.

Contrastive loss: One key component is a contrastive loss, inspired by the CLIP framework, which ensures alignment between the fusion module’s output and the text encoded by the CLIP text encoder. This strategy allows the fusion model to effectively learn how to align its fused vision tokens with the semantically rich text tokens generated by the lightweight CLIP text encoder.

Similar to the CLIP loss, the contrastive loss is applied to the $\langle \text{eos} \rangle$ token, a special marker indicating the end of an answer. In our case, the fusion module is designed to handle multiple question-answer pairs simultaneously. For questions and learnable queries, a single input sample may contain multiple groups of questions, each paired with its corresponding learnable queries. Within each group, the final token is designated as $\langle \text{eos} \rangle$ to indicate the boundary of that group. For answers, each answer is independently encoded, with the final token of each encoded answer also marked as $\langle \text{eos} \rangle$. The contrastive loss is computed specifically on these $\langle \text{eos} \rangle$ tokens, ensuring alignment between the fused representations of the question groups and their respective answers.

In addition to the $\langle \text{eos} \rangle$ tokens, the learnable queries contain other tokens that are not designated as $\langle \text{eos} \rangle$. For these tokens, we apply an identity loss to enforce orthogonality among them. This design encourages the non- $\langle \text{eos} \rangle$ tokens to encode as much distinct and

complementary information as possible, enhancing their ability to capture diverse features relevant to the task.

Let $\Omega_{\langle|\text{eos}|\rangle}$ denote the index set of $\langle|\text{eos}|\rangle$ tokens. For $i, j \in \Omega_{\langle|\text{eos}|\rangle}$, let \mathbf{v}_i represent the fused vision token corresponding to the $\langle|\text{eos}|\rangle$ token for the i -th question-answer pair, and let \mathbf{s}_j denote the answer text token associated with the $\langle|\text{eos}|\rangle$ token for the j -th question-answer pair. In addition, let $\bar{\Omega}_{\langle|\text{eos}|\rangle}$ represent the index set of non- $\langle|\text{eos}|\rangle$ tokens within the fused vision tokens. For these tokens, define \mathbf{Y} as a matrix where each row corresponds to a non- $\langle|\text{eos}|\rangle$ token, normalized to have an L2 norm of 1. Formally, each row is defined as $\mathbf{Y}_i = \mathbf{y}_i / \|\mathbf{y}_i\|_F$, where $i \in \bar{\Omega}_{\langle|\text{eos}|\rangle}$.

The contrastive loss, $\mathcal{L}_{\text{cont}}$, is defined as:

$$\mathcal{L}_{\text{cont}} = \frac{-1}{|\Omega_{\langle|\text{eos}|\rangle}|} \sum_{k \in \Omega_{\langle|\text{eos}|\rangle}} \log \left(\frac{\exp(\mathbf{v}_k^T \mathbf{s}_k)}{\sum_{i, j \in \Omega_{\langle|\text{eos}|\rangle}} \exp(\mathbf{v}_i^T \mathbf{s}_j)} \right) + \frac{1}{|\bar{\Omega}_{\langle|\text{eos}|\rangle}|} \|\mathbf{Y}^T \mathbf{Y} - I\|_F^2, \quad (19)$$

where I is the identity matrix corresponding to the dimension of $\mathbf{Y}^T \mathbf{Y}$.

Once the parameters of the fusion module have been adequately warmed up through preliminary training, the generation loss is introduced to empower the model’s capacity to generate accurate answers.

Generation Loss: Another essential component of our training framework is the generation loss, designed to ensure that the large language model generates accurate and contextually appropriate textual answers. This loss is implemented as a standard cross-entropy loss, a widely used approach in language modeling tasks.

In this task, the large language model is required to predict the correct answer. To achieve this, the loss function specifically targets the answer tokens, $\langle|\text{ans}|\rangle$, and the $\langle|\text{eos}|\rangle$ tokens, which mark the end of each answer. Let $\Omega' = \Omega_{\langle|\text{ans}|\rangle} \cup \Omega_{\langle|\text{eos}|\rangle}$ represent the combined index set of answer tokens and $\langle|\text{eos}|\rangle$ tokens. For each $i \in \Omega'$, denote the output logit from the language model for the i -th token as \mathbf{x}_i , where \mathbf{x}_{i, y_i} corresponds to the logit for the true token y_i , and $\mathbf{x}_{i, c}$ corresponds to the logit for a candidate token c . The cross-entropy loss is then defined as:

$$\mathcal{L}_{\text{ce}} = -\frac{1}{|\Omega'|} \sum_{i \in \Omega'} \log \frac{\exp(\mathbf{x}_{i, y_i})}{\sum_c \exp(\mathbf{x}_{i, c})}. \quad (20)$$

5 Experiments

In this section, we present the experimental results². For a detailed description of the dataset employed, please refer to Appendix B. The training process begins with a base model configured with $N_l = 256$ and $N_s = 8$, trained on the complete dataset. Subsequently, the model is fine-tuned using 10% subsets of the data with alternative configurations of N_l and N_s . Additional implementation details can be found in Appendix C.

To evaluate the performance of our model across various benchmarks, we utilize the VLMEvalKit (Duan et al., 2024). The evaluation encompasses a multitude of benchmarks, including MME (Fu et al., 2023), HallusionBench (Guan et al., 2024), POPE (Li et al., 2023c), and others. Various configuration of N_l and N_s are included in the evaluation,

2. The code is available at <https://github.com/tenghuilee/ScalingCapFusedVisionLM.git>

768(8), 512(8), 384(8), 256(8), 128(8), 64(8), 32(8), 16(8), 8(8), 1(1), where the first number represents N_l and the second number in parentheses denotes N_s . For a comprehensive presentation of the results across various benchmarks, please refer to Appendix D. Additionally, demonstrations are provided in Appendix F.

5.1 Scaling Analysis of Model Performance

In the following, we investigate the scaling properties of model performance with respect to the number of vision tokens N_l . To achieve this, we employ a scaling law analogous to the one proposed in (Kaplan et al., 2020). The relationship between the performance metric $S(N_l)$ and the number of vision tokens N_l is expressed as follows:

$$S(N_l) \approx \left(\frac{c}{N_l} \right)^\alpha, \quad (21)$$

where c and α are task-specific parameters that are estimated for each benchmark. The parameter c reflects the baseline performance of the model, while α determines the rate at which performance changes as a function of token count. Smaller α values indicate slower degradation in performance with token reduction, while larger α values signify a more pronounced impact. The insights derived from the fitted curves offer valuable guidance for optimizing vision-language models. Understanding the scaling dynamics could help to balance computational resources with desired performance levels effectively. For a detailed visualization of the related results, please refer to Appendix E.

To improve numerical stability, we apply the logarithm to both N_l and $S(N_l)$, and fit the data via the following mean square optimization problem:

$$\operatorname{argmin}_{\alpha, z} \frac{1}{|\Omega_{N_l}|} \sum_{n \in \Omega_{N_l}} (z - \alpha \log(n) - \log(S(n)))^2, \quad (22)$$

where $|\Omega_{N_l}|$ indicate the number of sampled points. Upon fitting, the constant c is derived as $c = e^{z/\alpha}$. Utilizing the default BFGS optimizer provided by SciPy, we fit the performance data to generate the curves illustrated in Figures 8 and 9, and the corresponding fitted parameters, c and α , are summarized in Table 1.

The fitted curves reveal a clear logarithmic relationship between the number of vision tokens N_l and performance across most benchmarks, regardless of whether the models incorporate the user’s questions as input. This trend aligns well with the theoretical scaling behavior described in Equation 21. The parameter α represents the slope of the logarithmic relationship, indicating the rate of performance improvement as the number of tokens increases. Across the benchmarks, α values are consistently negative, reflecting diminishing returns in performance gains as the token count grows larger.

Despite the general adherence to the scaling behavior, notable deviations are observed in some cases. For instance, the RealWorldQA benchmark presents a significant outlier, where the fitted curve deviates from the expected logarithmic trend. This deviation may result from domain-specific challenges or unique properties of the training data used in this benchmark.

In benchmarks such as OCRBench and ChartQA, steeper negative α values highlight that performance is more sensitive to the number of vision tokens. This indicates a stronger

SCALING CAPABILITY IN TOKEN SPACE

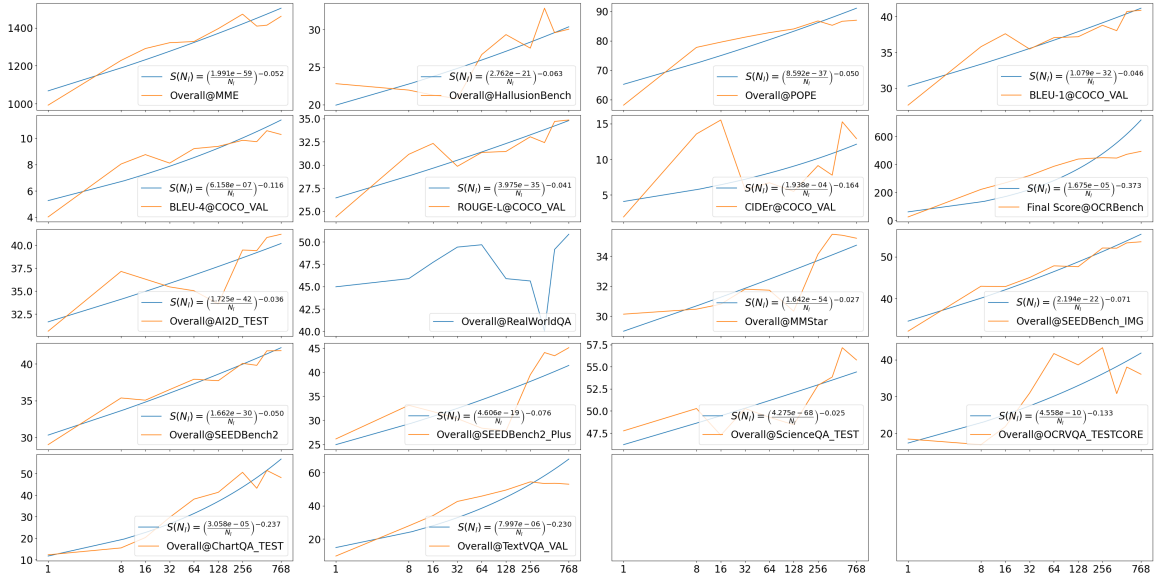


Figure 8: Scaling behavior of performances with respect to N_l . The models are taking vision tokens, user’s questions and learnable queries as input (“Vision Question Queries”). The x-axis in each subplot is log scaled, $\log_2(N_l)$.

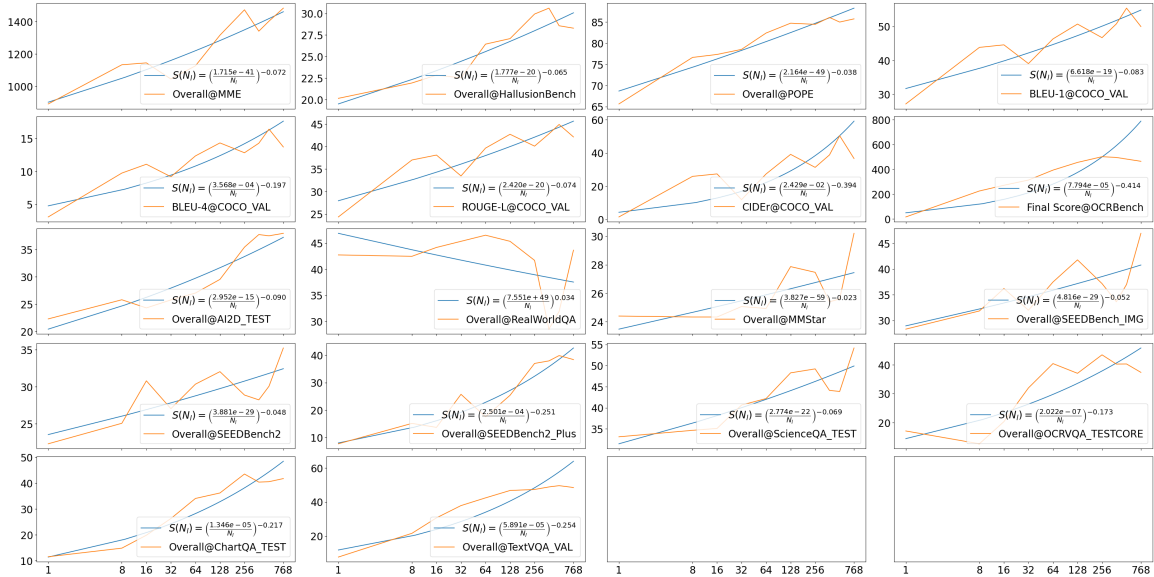


Figure 9: Scaling behavior of performances with respect to N_l . The further fine-tuned models are taking vision tokens and learnable queries as input (“Vision Queries (ft)”). The x-axis in each subplot is log scaled, $\log_2(N_l)$.

dependence on token count for these tasks, where reducing tokens could lead to substantial performance drops. Conversely, benchmarks like ScienceQA TEST and MMStar exhibit relatively flat α values, suggesting that performance is less sensitive to token scaling.

Table 1: The fitted scaling parameters, c, α , for each benchmark as illustrated in Figure 8 and Figure 9. The columns starting with “Vision Question Queries” are for models taking vision tokens, user’s questions and learnable queries as input. The columns starting with “Vision Queries (ft)” are for further fine-tuned models taking vision tokens and learnable queries as input. The blank cells indicate failed fits.

Benchmark	Vision Question Queries		Vision Queries (ft)	
	c	α	c	α
Overall@MME	1.9911e-59	-0.0516	1.7149e-41	-0.0725
Overall@HallusionBench	2.7617e-21	-0.0632	1.7770e-20	-0.0653
Overall@POPE	8.5924e-37	-0.0503	2.1636e-49	-0.0377
BLEU-1@COCO VAL	1.0786e-32	-0.0463	6.6175e-19	-0.0826
BLEU-4@COCO VAL	6.1584e-07	-0.1161	3.5680e-04	-0.1968
ROUGE-L@COCO VAL	3.9747e-35	-0.0413	2.4199e-20	-0.0737
CIDEr@COCO VAL	1.9376e-04	-0.1642	2.4293e-02	-0.3937
Final Score@OCRBench	1.6755e-05	-0.3727	7.7939e-05	-0.4142
Overall@AI2D TEST	1.7248e-42	-0.0359	2.9519e-15	-0.0902
Overall@RealWorldQA			7.5513e+49	0.0335
Overall@MMStar	1.6421e-54	-0.0272	3.8265e-59	-0.0235
Overall@SEEDBench IMG	2.1937e-22	-0.0710	4.8157e-29	-0.0516
Overall@SEEDBench2	1.6624e-30	-0.0498	3.8808e-29	-0.0483
Overall@SEEDBench2 Plus	4.6058e-19	-0.0762	2.5006e-04	-0.2512
Overall@ScienceQA TEST	4.2754e-68	-0.0247	2.7737e-22	-0.0695
Overall@OCRVQA TESTCORE	4.5581e-10	-0.1326	2.0220e-07	-0.1734
Overall@ChartQA TEST	3.0580e-05	-0.2370	1.3465e-05	-0.2173
Overall@TextVQA VAL	7.9968e-06	-0.2297	5.8912e-05	-0.2538

The constant c , derived from the fitted curves, provides an additional perspective on baseline performance. Higher values of c correspond to benchmarks with inherently stronger initial performance, even with fewer tokens. For example, benchmarks such as HallusionBench and ScienceQA TEST exhibit larger c values, indicating robustness in initial model performance.

While the fitted curves are not perfect, they sufficiently capture the overall scaling behavior across different benchmarks. The variations in α and c highlight task-specific differences in sensitivity to token scaling, offering insights for optimizing model architectures. Future work could refine these fits further and explore the underlying causes of outliers like RealWorldQA, potentially incorporating additional features of the datasets and tasks to enhance the modeling of scaling dynamics.

Overall, the fitted curves underscore the scaling capabilities of vision-language models and provide a foundation for developing strategies to balance computational efficiency with task-specific performance.

The observed scaling behavior across various benchmarks aligns with the theoretical results derived from the upper bound proposed in Section 3. Building upon the theoretical foundation, an upper bound for the distance between two branches is derived as:

$$\mathcal{O}\left(\sqrt{\psi(N)N^2 + (1 - \psi(N))N}\right).$$

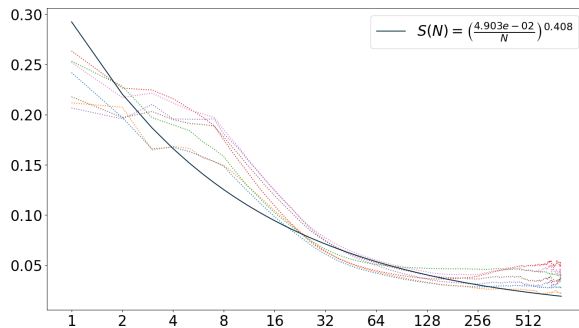


Figure 10: Fitted scaling curve of the estimated $\psi(N)$ function as illustrated in Figure 3a. The dashed lines represent the theoretical $\psi(N)$, while the solid line denotes the fitted curve based on empirical data. The fitting process utilized data within the range $N \in [1, 256]$. The fitted parameters are $c = 4.9030\text{e-}02, \alpha = 0.4079$. The x-axis is log-scaled, representing $\log_2(N)$.

The behavior of this upper bound is primarily governed by the $\psi(N)$ function. To elucidate the scaling dynamics, we aim to fit the $\psi(N)$ function with the observed scaling curves. Recall the estimated $\psi(N)$ for several large language models under the DPO dataset from Subsection 3.5. Following the similar optimization process as in objective function 22, we perform the fitting using the following optimization problem:

$$\operatorname{argmin}_{\alpha, z} \frac{1}{NM} \sum_{i=1}^M \sum_{n=1}^N (z - \alpha \log(n) - \log(\psi_i(n)))^2, \quad c = e^{z/\alpha}. \quad (23)$$

where $\psi_i(n)$ represents the $\psi(N)$ function of the i -th model. Figure 10 illustrates the fitted scaling curve of the $\psi(N)$. The solid line represents the empirical fit based on the optimization process, while the dashed lines denote the estimated $\psi(N)$ under different large language models. The fitted scaling curves reveal that the performance metrics adhere to the expected scaling behavior described in Equation 21.

The behavior of $\psi(N)$ and $S(N_l)$ exhibits a contrasting relationship. A smaller value of $\psi(N)$ corresponds to improved performance, whereas a larger value of $S(N_l)$ indicates better performance. As a result, the slopes of the lines in Figure 10 are inversely related to those shown in Figures 8 and 9. Despite this inverse relationship, the underlying scaling behavior remains consistent across the analyses. This consistency underscores the complementary nature of $\psi(N)$ and $S(N_l)$ as two perspectives on the scaling dynamics of the model’s performance.

In summary, the analysis reveals two insights: (1) The model demonstrates the scaling capability, $S(N_l) \approx (c/N_l)^\alpha$, and (2) The inclusion or exclusion of the user’s question in the input does not significantly affect the scaling capability.

5.2 Fusion With User’s Questions on Performance

In the majority of cases, it can be observed that fusing the text questions tokens from user do help improving the performance of the model. In the following, we will compare the

performances of the models with and without the fusion of the text questions taken from user.

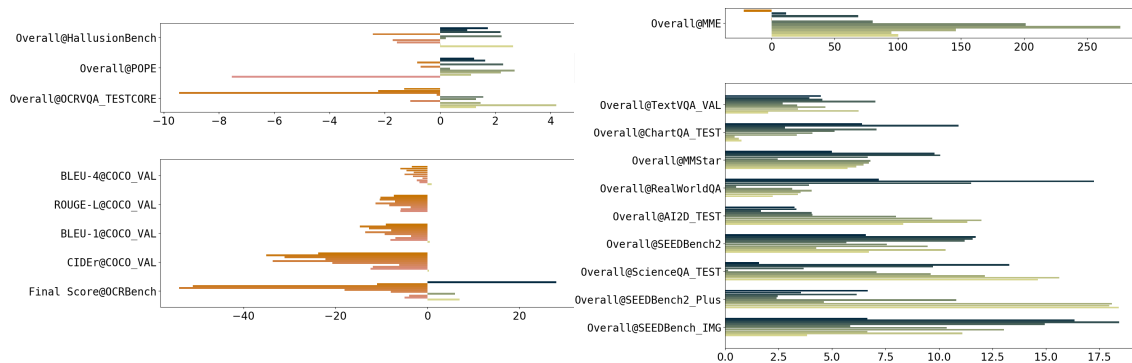


Figure 11: A horizontal bar plot on the performance differences $S_{vqq} - S_{vq\ ft}$ for different benchmarks, where S_{vqq} is the model with user’s questions and $S_{vq\ ft}$ is the further fine-tuned model without user’s questions. Each benchmark is represented as a separate plot, and within each plot, the horizontal bars correspond to $N_l = 1, 8, \dots, 768$, ordered from top to bottom.

Let S_{vqq} denote the performance value of the models that incorporate the user’s question as part of the input. For comparison, the model was further refined without the user’s question as part of the input, as outlined in Appendix C. Let $S_{vq\ ft}$ represent the performance value of the fine-tuned models that exclude the user’s question. The performance difference between the two models, $S_{vqq} - S_{vq\ ft}$, is visualized as horizontal bar plots in Figure 11. For each horizontal bar plot, the color represents the performance difference $S_{vqq} - S_{vq\ ft}$. If the value is positive ($S_{vqq} - S_{vq\ ft} > 0$), the bar is colored green, indicating that the model incorporating the user’s question outperforms the fine-tuned model without the question. Conversely, if the value is negative ($S_{vqq} - S_{vq\ ft} < 0$), the bar is colored red, indicating that the fine-tuned model without the question achieves better performance than the model with the question.

From Figure 11, we observe that the green areas are larger than the red areas for most benchmarks. However, in some benchmarks, the red areas dominate, indicating that the fine-tuned model without the user’s question performs better. This highlights that the effectiveness of incorporating the user’s question is highly dependent on whether the question provides meaningful context to generate the correct answer.

For example, questions that direct the model’s attention to a specific part of the image, such as “In the given image, what is located in the left corner?”, can enhance performance by helping the model focus on relevant regions. In contrast, general questions that require holistic understanding, such as “Please describe the image in detail”, may not provide any additional benefit. In some cases, they may even hinder performance by encouraging the model to focus unnecessarily on specific regions instead of processing the image as a whole. Therefore, the model with the user’s question can achieve better performance. Some opposite examples are the sores from COCO VAL benchmark, which show more red areas than green. This benchmark involves question: “Please describe this image in general.

Directly provide the description, do not include a prefix like ‘This image depicts’.’, requiring comprehensive descriptions of images. Here, the user’s question does not effectively aid the fusion model in achieving better performance, as the task demands a global understanding of the image rather than focusing on specific regions.

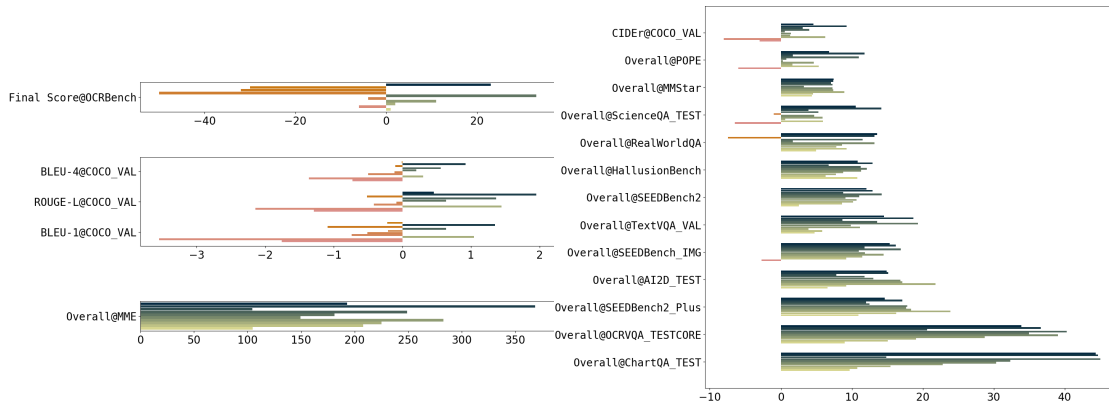


Figure 12: A horizontal bar plot on the performance difference $S_{vqq} - S_{vq}$ for each benchmark, where S_{vqq} is the model with user’s questions and S_{vq} is the model without user’s questions. Each benchmark is represented as a separate plot, and within each plot, the horizontal bars correspond to $N_l = 1, 8, \dots, 768$, ordered from top to bottom.

In the previous comparison, the model excluding the user’s question as part of the input was further fine-tuned before evaluation. To provide a more direct comparison, we now evaluate the model without the user’s question directly, without applying any additional fine-tuning. This approach allows us to determine whether the user’s question is effectively utilized by the model and to assess the inherent impact of including the user’s question on performance.

Let S_{vq} denote the performance of the model without incorporating the user’s question as input and without any fine-tuning. The performance difference, $S_{vqq} - S_{vq}$, is computed for each benchmark and visualized in Figure 12. The color convention in this figure follows the same scheme as in Figure 11, where green bars indicate $S_{vqq} > S_{vq}$ and red bars indicate $S_{vqq} < S_{vq}$. From Figure 12, we observe that more green bars are present compared to red bars, suggesting that the model with the user’s question generally outperforms the model without the user’s question. Additionally, the relative performance range shown on the right-hand side of Figure 12 spans $[0, 40]$, which is significantly larger than the range observed in Figure 11 ($[0, 17]$). This indicates that in these benchmarks, the model relies heavily on the user’s questions to achieve better performance.

Similar to Figure 11, there are some outliers in Figure 12, suggesting that under some specific conditions, the model without the user’s question can slightly perform better than the model with the user’s question.

In summary, the under most cases, fusing the user’s question into the input of the model can improve its performance if the question is relevant to the task.

5.3 Compare to The Baseline Models

The performance of our model is comparable to the baseline models on some benchmarks.

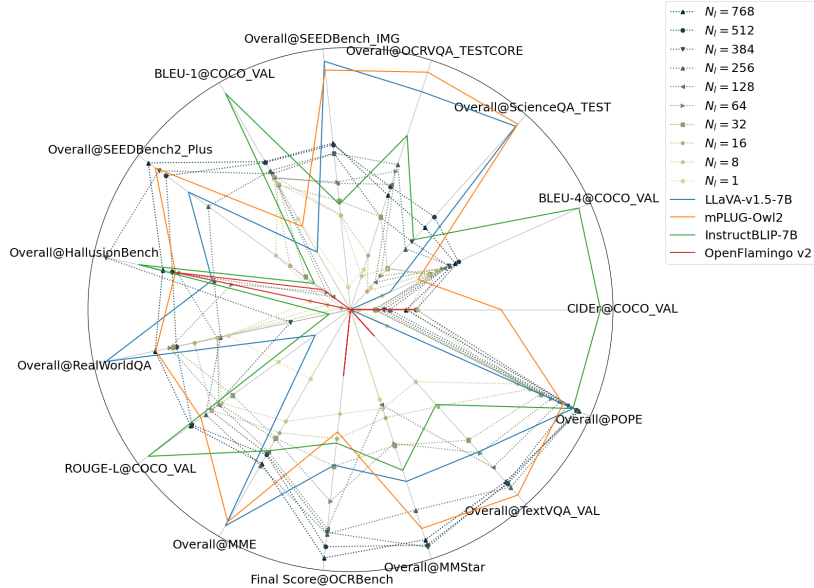


Figure 13: Comparison of the proposed models and the baseline models on various benchmarks. For each benchmark, the performance is scaled to $[0, 1]$ via the projection $\mathbf{x} \leftarrow (\mathbf{x} - \min(\mathbf{x})) / (\max(\mathbf{x}) - \min(\mathbf{x}))$. Results of baseline models are taken from VLMEvalKit.

We consider the following baseline models for comparison: LLaVA-v1.5-7B (Liu et al., 2023a), mPLUG-Owl2 (Ye et al., 2023b), and InstructBLIP-7B (Dai et al., 2023) and OpenFlamingo v2 (Alayrac et al., 2022). It is important to note that these models were not trained on the same dataset as our proposed model. As a result, the comparisons are not directly equivalent and are provided for reference purposes only. The performance of these baseline models, alongside our model, is presented in Figure 13. The dashed line in Figure 13 represents the various configurations of our model. Based on previous discussions, as N_l increases, the performance of our model improves. Here, we focus on comparing the best performance of our model with the baseline models. Our model demonstrates comparable performance to the baseline models on several benchmarks, such as OCRBench, MMStart POPE, SEEDBench2 Plus, and HallusionBench. However, on other benchmarks, such as ScienceQA Test, SeedBench IMG, RealWorld QA, and MME, our model underperforms relative to the baseline models.

Overall, the performance of our model is comparable to the baseline models on some benchmarks, but it underperforms on others.

6 Conclusion and Future Work

In this study, we examined the impact of incorporating vision tokens and a fusion mechanism that integrates the user’s question with large vision language models under fifteen diverse

benchmarks. Our empirical analysis demonstrates that the model exhibits a scaling behavior characterized by the relationship $S(N_l) \approx (c/N_l)^\alpha$, where N_l represents the number of vision tokens, α shows the rate of performance changes, and c is a task related value. Moreover, we also analysis the effect of the fusion mechanism that integrates the user’s question with the vision tokens. The results revel two important findings. First, the scaling behavior remains largely unaffected by the inclusion or exclusion of the user’s question in the input. Second, the fusion mechanism significantly enhances model performance when the question is task-specific and contextually relevant.

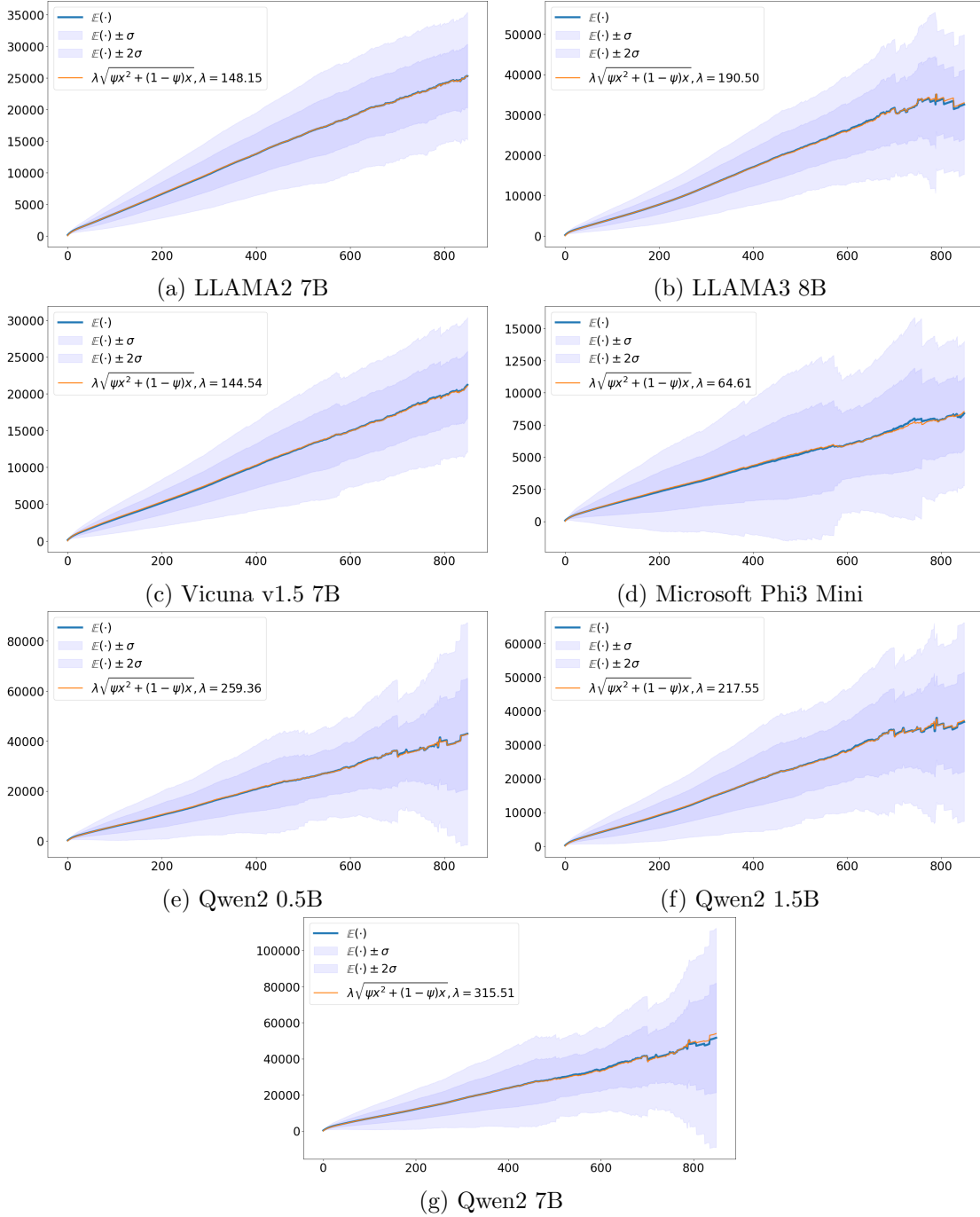
Despite these findings, our study has several limitations. Firstly, the observed scaling behavior is restricted to a specific range of vision token counts, leaving open questions about the model’s performance under extreme conditions or beyond this range. Secondly, the additional fine-tuning applied to the model with $N_l = 256, N_s = 8$, using only 10% of the dataset after the training on the full dataset. This strategy may introduce bias and limit the generalizability of our results. Lastly, all training and fine-tuning operations were performed solely on the vision tokens, while the large language model was kept frozen. This approach may affect the generalizability of our findings in situations where the language model is fine-tuned.

In future work, we aim to address these limitations and try to extend our findings to a broader range of vision token counts and model configurations.

Acknowledgments and Disclosure of Funding

Appendix A. Illustration of The Theoretical Upper Bound

Complementing the theoretical analysis, we present visual illustrations of the theoretical upper bounds across various large language models.



Appendix B. Datasets

Our model training utilizes a combination of existing datasets and newly generated data to enhance performance across various tasks. The primary datasets employed include LLAVA V1.5 MIX665K (Liu et al., 2023a), BAAI-SVIT (Zhao et al., 2023), and mPLUG DocDownstream 1.0 (Ye et al., 2023a).

To further augment the training data, we generated new question-and-answer pairs using detailed descriptions from BAAI-SVIT, with the Llama-3 8B model serving as the agent. The generated questions were of two types: yes/no questions and multiple-choice questions (e.g., selecting one option from A, B, C, or D). To maintain data quality, any generated text that did not conform to the correct format was excluded from the dataset.

Another source of augmented training data comes from the structure-aware parsing task in CCpdf, derived from mPLUG DocDownstream 1.0. To enhance data quality, we utilized the nougat-base model (Blecher et al., 2024) to convert a subset of images into better-formatted text. To ensure the validity of the outputs, we applied several filtering criteria: (1) generated texts that were too short were discarded, (2) cases where the length difference between the original and generated text was excessively large were excluded, (3) generated texts containing endless repeated patterns were removed, and (4) texts that lacked sufficient similarity to the original under the embedding space, as measured using all-mpnet-base-v2 (Reimers and Gurevych, 2019), were filtered out. These steps ensured that the final dataset maintained high quality and relevance for training.

Appendix C. Implementation Details

Our implementation is built upon two widely used open-source pretrained models: CLIP ViT-H/14 (Radford et al., 2021) and Llama-2 7B (Touvron et al., 2023b). The CLIP ViT-H/14 vision encoder processes image inputs with a resolution of (336, 336), using a stride of 14, resulting in $24 \times 24 = 576$ tokens, each with a hidden size of 1024. The Llama-2 7B model, serving as the backbone language model, features a hidden size of 4096.

The experiments were conducted on high-performance hardware comprising 8 NVIDIA A100 GPUs, each with 40 GB of memory. For evaluation on more accessible hardware, we utilized NVIDIA RTX A6000 GPUs, each with 48 GB of memory.

The image preprocessing pipeline involves several steps to adapt raw pixel images for input to the CLIP vision encoder. First, as introduced in subsection 4.2, the images are processed into global and local views, with each view independently passed through the CLIP encoder to generate vision tokens.

Based on the available hardware resources, we adopt an HD-9 cropping strategy, which generates nine local image views and one global image view as input to the CLIP vision encoder. Each view has a resolution of (336, 336), resulting in a maximum input image resolution of (1008 × 1008). This setup initially produces 5760 tokens, which is computationally expensive to process. To address this, we apply a local merging operation that reduces the token count by a factor of four. Neighboring vision tokens are merged in a $4 \times 4 \Rightarrow 1$ manner using a 2D convolution with a kernel size of 3, padding of 1, and a stride of 2. This reduces the vision token count to 1440. After appending $\langle \text{new line} \rangle$ tokens to mark the end of each

view, the total token count becomes 1450. The tokens for all views are then concatenated, ensuring efficient processing while retaining critical information.

As introduced in subsection 4.2, the fused model integrates the vision tokens from the global and local views with the text tokens from the user’s question and the learnable queries. For the first question, N_l learnable queries are appended, while subsequent questions are each followed by N_s learnable queries. The value of N_l ranges from 1 to 768, with N_s set to 8 when $N_l \geq 8$. For smaller values of N_l (i.e., $N_l < 8$), N_s is set equal to N_l . For example, when only one learnable query is used, both N_l and N_s are set to 1. The text tokenizer is based on the CLIP text tokenizer, and N_l new special tokens are added to the tokenizer to support the learnable queries.

The hidden size of the fused model is set to 1024, matching the hidden size of the vision tokens generated by CLIP ViT-H/14. This is significantly smaller than the hidden size of Llama-2 7B, which is 4096. Adopting a smaller hidden size helps reduce both memory consumption and computational cost, making the model more efficient for training and inference.

To align the fused vision tokens generated by the fused model with the Llama-2 7B backbone, a linear projection layer is used to map the fused vision tokens to the hidden size of the Llama-2 model. We consider a three-step training strategy for optimizing the model.

In the first step, we perform preliminary training using the contrastive loss introduced in Equation 19 to align the fused vision tokens with the CLIP text encoder. Since the maximum sequence length of the CLIP text encoder is 77 and most questions exceed this limit, we extend the sequence length to 512 to accommodate longer inputs. The modules involved in this step include the vision encoder, the 2D convolution layer for merging neighboring vision tokens, the fused model, and the CLIP text encoder. This step requires only a few training steps, using a batch size of 32 per device, gradient accumulation of 1, an equivalent batch size of 256, and a learning rate of $2e-5$. The training employs a cosine learning rate scheduler with a warm-up ratio of 0.1 and is performed over 1000 steps.

The second step involves fine-tuning on the full dataset. The required modules include the vision encoder, the 2D convolution layer, the fused model, a linear projection layer to map the fused vision tokens to the Llama-2 hidden size, and the Llama-2 7B backbone. In this stage, the Llama-2 backbone is frozen, and the remaining modules are updated. The training uses a batch size of 5 per device, gradient accumulation of 64, and an equivalent batch size of 2560, with a learning rate of $2e-5$. A cosine learning rate scheduler with a warm-up ratio of 0.03 is employed. The training spans two epochs and uses the generation loss described in Equation 20. The fusion model consists of 20 layers, with $N_l = 256$ learnable queries for the first question and $N_s = 8$ for subsequent questions. Given the considerable size of the dataset, the fine-tuning process is estimated to require more than 200 hours.

The third step focuses on further fine-tuning to evaluate various configurations of N_l and N_s , such as $N_l = 128, N_s = 8$ and $N_l = 64, N_s = 8$. To reduce the substantial time required for full-data fine-tuning, we reuse the model trained in the second step ($N_l = 256, N_s = 8$) and fine-tune it using only 10% of randomly sampled training data, which will take approximately 10 hours. This includes fine-tuning for alternative configurations as well as the original $N_l = 256, N_s = 8$. This strategy significantly reduces computational cost while allowing for the exploration of multiple settings. The loss function remains the same

as in the second step (Equation 20), with the Llama-2 backbone frozen and updates applied only to the other modules. All other hyperparameters and configurations are consistent with those used in the second step.

Another critical aspect of the fusion model is assessing the impact of incorporating the user’s question on the model’s performance. To evaluate this, we introduce an alternative setup where the model processes inputs without including the user’s question. In this configuration, the input is limited to vision tokens and learnable queries, excluding any text-based queries provided by the user. To determine the validity of fusing the user’s question, we conduct experiments both with and without further fine-tuning the model, keeping the Llama-2 backbone frozen in both cases. For this evaluation, we reuse the 10% randomly sampled training data previously employed for tuning different configurations of N_l . All other hyperparameters and configurations are kept consistent with those used in the second step. This approach allows us to efficiently analyze the influence of the user’s question on the fusion model’s performance while maintaining computational efficiency.

Appendix D. Detailed Results

For evaluation, we utilize the VLMEvalKit (Duan et al., 2024) to compute scores across various benchmarks. Different configurations of N_l and N_s are tested, including: 768(8), 512(8), 384(8), 256(8), 128(8), 64(8), 32(8), 16(8), 8(8), 1(1), where the first number represents N_l and the second number in parentheses denotes N_s . The losses and gradient norms of the further fine-tuned models are shown in Figure 15.

The evaluation spans a diverse set of benchmarks, including MME (Fu et al., 2023), HallusionBench (Guan et al., 2024), POPE (Li et al., 2023c), OCRBench (Liu et al., 2023b), COCO VAL (Lin et al., 2014), RealWorldQA³, MMStar (Chen et al., 2024a), SEEDBench IMG (Li et al., 2024b), SEEDBench2 (Li et al., 2023a), SEEDBench2 Plus (Li et al., 2024a), ScienceQA TEST (Lu et al., 2022), AI2D TEST⁴, OCRVQA TESTCORE (Mishra et al., 2019), ChartQA TEST (Masry et al., 2022), and TextVQA VAL (Singh et al., 2019).

The baseline models are: 360VL-70B⁵, InstructBLIP-7B (Dai et al., 2023), InternLM-XComposer2-4KHD (Dong et al., 2024), LLaVA-v1-7B, LLaVA-v1.5-13B, LLaVA-v1.5-7B (Liu et al., 2023a), MiniGPT-4-v1-7B, MiniGPT-4-v2 (Zhu et al., 2024), mPLUG-Owl2 (Ye et al., 2023b), OpenFlamingo v2 (Alayrac et al., 2022), Phi-3-Vision (Abdin et al., 2024), Qwen-VL-Chat (Bai et al., 2023b).

The results are summarized in the following tables, with all benchmark data for the models obtained from VLMEvalKit (Duan et al., 2024). The blank cells indicate that the scores are not available from VLMEvalKit.

In the column titled “Fused Model Inputs,” the following terms are used to describe the input configurations of the model:

- “Vision Query Queries” refers to the model that takes vision tokens, text tokens from the user’s question, and learnable queries as inputs.

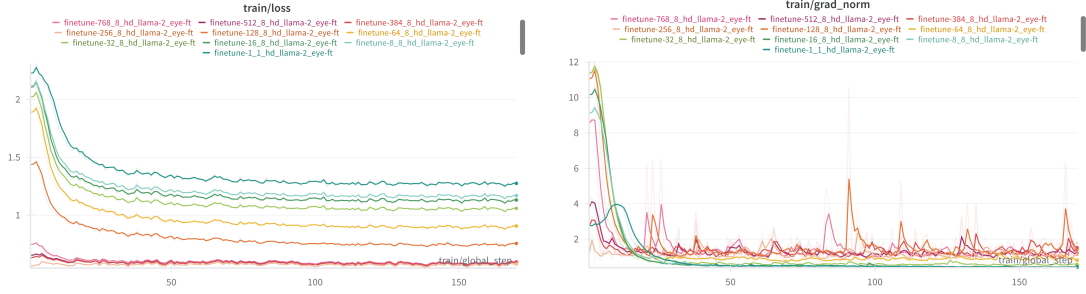
3. <https://x.ai/blog/grok-1.5v>

4. <https://allenai.org/data/diagrams>

5. <https://github.com/360CVGroup/360VL>

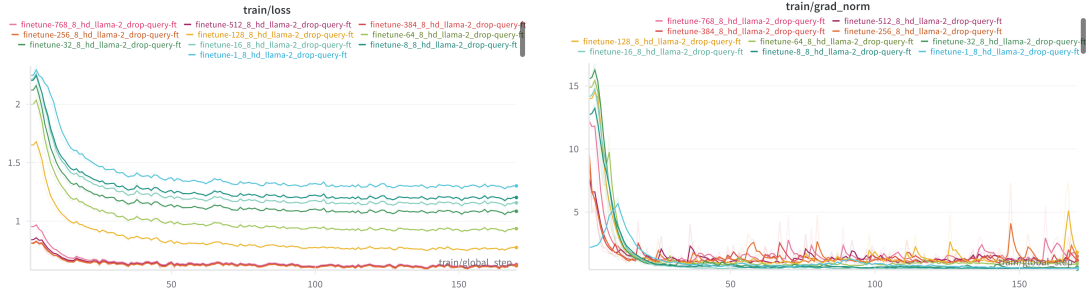
- “Vision Query (ft)” refers to the model that takes vision tokens and learnable queries as inputs, with the model further fine-tuned without the user’s question.
- “Vision Query” refers to the model that takes vision tokens and learnable queries as inputs, but remains the same as the original model, without any additional fine-tuning.

It is important to note that the training datasets for these models differ, and as such, the results are provided for reference purposes only.



(a) Losses of “Vision Query Queries”.

(b) Gradient norms of “Vision Query Queries”.



(c) Losses of “Vision Query (ft)”.

(d) Gradient norms of “Vision Query (ft)”.

Figure 15: Losses and gradient norms of further fine-tune model with different configurations.

Table 2: POPE

Fused Model Inputs	N_l	Overall	acc	precision	recall
Vision Question Queries	768	86.977	87.033	87.357	86.600
Vision Queries (ft)	768	85.742	85.456	84.085	87.467
Vision Queries	768	80.158	76.500	69.362	94.933
Vision Question Queries	512	86.626	86.444	85.482	87.800
Vision Queries (ft)	512	84.990	84.400	81.891	88.333
Vision Queries	512	74.835	66.978	60.451	98.200
Vision Question Queries	384	85.254	84.433	80.984	90.000
Vision Queries (ft)	384	86.080	86.233	87.048	85.133
Vision Queries	384	83.572	82.178	77.508	90.667
Vision Question Queries	256	86.734	87.233	90.267	83.467
Vision Queries (ft)	256	84.447	83.289	78.975	90.733
Vision Queries	256	75.719	68.767	61.933	97.400
Vision Question Queries	128	84.016	82.878	78.778	90.000
Vision Queries (ft)	128	84.727	84.822	85.261	84.200
Vision Queries	128	83.255	82.522	80.331	86.400
Vision Question Queries	64	82.761	81.489	77.440	88.867
Vision Queries (ft)	64	82.398	80.756	76.029	89.933
Vision Queries	64	82.476	81.756	79.343	85.867
Vision Question Queries	32	81.232	80.300	77.562	85.267
Vision Queries (ft)	32	78.539	74.278	67.377	94.133
Vision Queries	32	76.593	78.933	86.167	68.933
Vision Question Queries	16	79.533	77.200	72.150	88.600
Vision Queries (ft)	16	77.338	72.944	66.533	92.333
Vision Queries	16	77.879	75.800	71.717	85.200
Vision Question Queries	8	77.749	74.167	68.280	90.267
Vision Queries (ft)	8	76.634	71.933	65.734	91.867
Vision Queries	8	72.383	63.422	58.140	95.867
Vision Question Queries	1	58.113	49.689	49.778	69.800
Vision Queries (ft)	1	65.648	52.033	51.134	91.667
Vision Queries	1	64.091	58.678	56.679	73.733
Model Name					
LLaVA-v1.5-13B		88.400	88.600	89.600	87.300
360VL-70B		87.300	88.200	94.700	81.100
LLaVA-v1.5-7B		86.100	87.000	92.100	80.900
InstructBLIP-7B		86.100	86.000	85.700	86.500
mPLUG-Owl2		84.600	85.400	89.800	79.900
Phi-3-Vision		83.700	85.600	96.100	74.100
LLaVA-v1-7B		75.900	69.200	62.300	96.900
Qwen-VL-Chat		74.900	67.300	67.800	83.600
MiniGPT-4-v2		60.000	48.400	49.900	75.300
OpenFlamingo v2		52.600	42.400	50.000	55.500
MiniGPT-4-v1-7B		34.600	36.400	58.400	24.600
InternLM-XComposer2-4KHD		2.900	10.100	53.700	1.500

Table 3: Combination scores of MME, HallusionBench, COCO VAL.

Fused Model Inputs	N_l	MME			HallusionBench				COCO VAL			
		Overall	Perception	Cognition	aAcc	fAcc	qAcc	Overall	BLEU-1	BLEU-4	ROUGE-L	CIDEr
Vision Question Queries	768	1461.206	1202.635	258.571	50.683	22.254	17.143	30.027	40.892	10.282	34.858	12.897
Vision Queries (ft)	768	1483.059	1244.845	238.214	50.053	18.786	16.044	28.294	49.980	13.713	42.126	36.652
Vision Queries	768	1268.119	1072.405	195.714	34.805	12.428	10.330	19.188	41.113	10.291	34.400	8.308
Vision Question Queries	512	1414.270	1165.699	248.571	50.578	21.387	16.703	29.556	40.707	10.570	34.702	15.256
Vision Queries (ft)	512	1402.772	1182.058	220.714	51.314	17.052	17.363	28.576	55.407	16.420	44.891	50.358
Vision Queries	512	1045.693	860.693	185.000	29.232	10.694	9.890	16.605	39.360	9.647	32.752	6.008
Vision Question Queries	384	1409.437	1152.294	257.143	54.784	21.676	21.978	32.813	38.037	9.740	32.416	7.763
Vision Queries (ft)	384	1340.833	1112.976	227.857	52.156	20.809	18.901	30.622	50.765	14.282	42.812	38.826
Vision Queries	384	1304.939	1085.296	219.643	46.057	15.607	16.484	26.049	39.129	9.844	32.932	4.672
Vision Question Queries	256	1472.529	1209.315	263.214	48.791	18.786	14.945	27.507	38.787	9.838	33.043	9.108
Vision Queries (ft)	256	1472.806	1225.663	247.143	50.473	21.098	18.242	29.938	46.695	12.835	40.083	31.333
Vision Queries	256	1223.633	1018.990	204.643	30.284	10.116	8.352	16.250	38.147	9.280	31.678	5.103
Vision Question Queries	128	1396.146	1157.574	238.571	51.104	18.786	18.022	29.304	37.189	9.383	31.461	5.491
Vision Queries (ft)	128	1315.989	1095.632	220.357	49.527	15.896	15.824	27.082	50.710	14.330	42.714	39.148
Vision Queries	128	1215.086	1001.872	213.214	32.492	10.983	8.132	17.202	37.400	9.181	30.822	4.903
Vision Question Queries	64	1328.092	1095.235	232.857	48.160	16.185	15.604	26.650	37.055	9.207	31.348	6.703
Vision Queries (ft)	64	1126.880	889.023	237.857	48.686	15.029	15.604	26.440	46.324	12.352	39.644	27.363
Vision Queries	64	1178.733	1003.733	175.000	30.599	8.960	6.374	15.311	37.565	9.321	31.435	5.299
Vision Question Queries	32	1321.832	1099.689	222.143	42.587	10.405	9.451	20.814	35.466	8.110	29.854	5.743
Vision Queries (ft)	32	1045.688	830.331	215.357	45.321	12.139	10.110	22.523	39.049	9.191	33.465	11.910
Vision Queries	32	1039.101	835.887	203.214	25.026	6.358	4.615	12.000	36.205	8.608	30.269	4.443
Vision Question Queries	16	1291.082	1066.082	225.000	43.113	13.006	7.692	21.270	37.606	8.754	32.330	15.509
Vision Queries (ft)	16	1145.157	938.729	206.429	44.585	12.717	11.209	22.837	44.580	11.090	38.103	27.403
Vision Queries	16	1066.146	889.003	177.143	27.340	8.382	4.835	13.519	36.562	8.452	30.886	9.226
Vision Question Queries	8	1228.312	992.954	235.357	42.482	13.873	9.451	21.935	35.793	8.040	31.152	13.552
Vision Queries (ft)	8	1133.447	905.590	227.857	42.376	13.295	10.110	21.927	43.824	9.748	37.006	25.907
Vision Queries	8	1020.312	841.383	178.929	34.490	5.491	6.813	15.598	39.338	9.401	33.294	21.574
Vision Question Queries	1	992.141	734.284	257.857	44.059	11.561	12.747	22.789	27.612	4.022	24.384	1.899
Vision Queries (ft)	1	891.690	679.190	212.500	41.956	10.116	8.352	20.141	27.142	3.086	24.364	1.516
Vision Queries	1	887.341	690.556	196.786	25.342	5.780	4.835	11.986	29.373	4.749	25.674	4.887
Model Name												
InternLM-XComposer2-4KHD		2130.400	1581.500	548.900	60.700	33.800	33.000	42.500	20.200	4.900	17.700	6.000
Qwen-VL-Chat		1860.000	1467.800	392.100	56.400	27.700	26.400	36.800	75.800	34.000	54.900	98.900
360VL-70B		2009.700	1646.200	363.600	54.600	26.900	23.100	34.800	71.000	28.100	53.000	86.600
mPLUG-Owl2		1786.400	1436.000	350.400	48.900	22.500	16.700	29.400	25.800	7.100	33.600	35.000
Phi-3-Vision		1508.000	1205.100	302.900	56.800	29.500	30.800	39.000	15.800	2.900	16.100	0.000
LLaVA-v1.5-7B		1808.400	1506.200	302.100	48.800	20.500	13.600	27.600	19.800	4.700	20.000	0.000
LLaVA-v1.5-13B		1780.800	1502.600	278.200	45.300	17.100	11.000	24.500	20.700	5.100	21.400	0.400
MiniGPT-4-v1-7B		1047.400	770.600	276.800	52.400	17.300	25.900	31.900	19.600	4.300	17.500	0.800
MiniGPT-4-v2		968.400	708.400	260.000	52.600	16.500	21.100	30.000	12.600	1.400	13.300	0.100
InstructBLIP-7B		1391.400	1137.100	254.300	53.600	20.200	19.800	31.200	56.800	20.900	39.900	58.100
LLaVA-v1-7B		1075.500	832.000	243.600	43.600	13.000	8.100	21.600	27.000	6.700	26.400	5.500
OpenFlamingo v2		607.200	535.000	72.100	52.700	17.600	18.000	29.400	6.400	1.300	15.800	14.900

Table 4: Combination scores of OCRBench, AI2D TEST, RealWorldQA, MMStar, SEED-Bench IMG, SEEDBench2, SEEDBench2 Plus, ScienceQA TEST, OCRVQA TESTCORE, ChartQA TEST, TextVQA VAL.

Fused Model Inputs	N_l	Final Score@OCRBench		Overall AI2D TEST		Overall RealWorldQA		Overall@MMStar		Overall@SEEDBench IMG		Overall@SEEDBench2		Overall SEEDBench2 Plus		Overall ScienceQA TEST		Overall OCRVQA TESTCORE		Overall@ChartQA TEST		Overall@TextVQA VAL	
		Overall	AI2D TEST	Overall	RealWorldQA	Overall@MMStar	Overall@SEEDBench IMG	Overall@SEEDBench2	Overall SEEDBench2 Plus	Overall ScienceQA TEST	Overall OCRVQA TESTCORE	Overall@ChartQA TEST	Overall@TextVQA VAL										
Vision Question Queries	768	493	41.192	50.850	35.200	53.598	41.804	45.059	55.776	36.068	48.160	52.998											
Vision Queries (ft)	768	465	37.953	43.660	30.200	46.944	35.230	38.384	54.189	37.370	41.760	48.522											
Vision Queries	768	470	26.295	37.255	27.733	38.245	29.761	30.391	45.216	2.181	3.800	38.474											
Vision Question Queries	512	472	40.835	49.150	35.400	53.338	41.775	43.390	57.164	38.021	51.480	53.550											
Vision Queries (ft)	512	483	37.500	31.895	25.600	37.001	30.064	39.833	43.877	40.267	40.560	49.612											
Vision Queries	512	502	25.712	35.948	28.000	37.149	28.825	26.263	42.985	1.367	6.800	34.884											
Vision Question Queries	384	445	39.411	40.000	35.467	52.066	39.806	44.049	53.842	30.794	43.200	53.400											
Vision Queries (ft)	384	496	37.727	28.497	25.400	33.635	28.222	37.901	44.125	40.234	40.400	48.856											
Vision Queries	384	477	31.574	47.451	28.400	40.289	31.004	32.060	49.926	10.189	28.320	44.720											
Vision Question Queries	256	448	39.475	45.621	34.133	52.108	40.072	39.438	52.900	43.294	50.600	54.396											
Vision Queries (ft)	256	502	35.427	41.699	27.467	37.170	28.874	36.978	49.232	43.424	43.520	47.370											
Vision Queries	256	498	27.655	34.118	26.867	35.216	25.838	26.921	47.595	3.027	5.600	40.820											
Vision Question Queries	128	438	33.614	45.882	30.333	47.625	37.713	27.800	48.438	38.607	41.320	49.472											
Vision Queries (ft)	128	456	29.534	45.359	27.867	41.779	32.034	25.384	48.290	37.044	36.200	46.774											
Vision Queries	128	405	20.596	44.183	27.067	36.615	26.683	9.969	49.430	3.646	9.000	30.138											
Vision Question Queries	64	386	35.039	49.673	31.733	47.829	37.914	28.371	49.281	41.699	38.160	45.802											
Vision Queries (ft)	64	394	27.040	46.536	24.933	37.472	30.343	17.567	42.191	40.397	34.080	42.438											
Vision Queries	64	390	18.199	36.471	24.467	35.954	28.797	10.716	44.571	2.637	7.800	35.918											
Vision Question Queries	32	320	35.460	49.412	31.800	45.025	36.507	30.347	50.273	30.924	29.680	42.600											
Vision Queries (ft)	32	314	25.777	45.359	25.067	31.984	27.032	25.736	40.654	31.999	26.320	37.910											
Vision Queries	32	309	18.329	40.784	24.400	30.516	25.830	11.989	44.373	2.214	6.840	31.434											
Vision Question Queries	16	268	36.302	47.712	30.800	42.854	35.066	31.796	47.248	21.810	20.320	34.112											
Vision Queries (ft)	16	272	24.320	44.183	24.333	36.207	30.795	13.702	35.102	20.345	19.880	30.708											
Vision Queries	16	266	14.508	39.869	21.867	31.366	24.890	7.905	46.653	2.734	4.840	30.236											
Vision Question Queries	8	221	37.144	45.882	30.467	42.938	35.370	33.114	50.273	16.895	15.520	27.886											
Vision Queries (ft)	8	226	25.810	42.484	24.333	31.844	25.058	15.152	34.655	12.695	14.880	21.636											
Vision Queries	8	227	27.947	36.601	25.933	33.699	26.765	16.864	44.323	1.823	4.760	22.032											
Vision Question Queries	1	24	30.635	44.967	30.133	32.153	29.022	26.131	47.744	18.424	12.320	9.708											
Vision Queries (ft)	1	17	22.312	42.745	24.400	28.309	22.289	7.729	33.118	17.122	11.560	7.694											
Vision Queries	1	23	24.028	40.000	25.733	34.865	26.474	15.195	54.239	9.440	2.640	4.930											
Model Name																							
InternLM-XComposer2-4KHD	675		63.300	55.300	74.600	57.400	65.200	96.300															
Phi-3-Vision	637		58.800	47.700	70.900	55.700	64.200	90.000	61.900	81.800	72.400												
Qwen-VL-Chat	488		49.300	34.500	64.800		46.000	68.800	58.600	49.800	60.700												
360VL-70B	397		62.400	48.100	73.100		52.300	87.400															
LLaVA-v1.5-13B	337		55.300	34.300	68.200		44.600	72.600	63.400	18.200	48.900												
LLaVA-v1.5-7B	318		54.800	33.100	65.800	43.400	41.300	69.200	60.600	17.800	45.500												
InstructBLIP-7B	276		36.900	32.700	44.500		29.500	54.100	50.200	10.900	33.600												
LLaVA-v1-7B	269		45.800	27.100	50.400		31.200	61.800															
mPLUG-Owl2	255		50.800	34.800	64.500		44.400	69.500	65.200	22.800	56.400												
MiniGPT-4-v1-7B	172		21.300	16.300	31.600		15.200	39.600	0.300		0.600												
OpenFlamingo v2	149		35.200	26.900	28.800		28.700	44.800	8.900		16.300												
MiniGPT-4-v2	31		30.700	21.300	29.400		23.300	54.700	0.000		0.000												

Appendix E. Further Analysis on N_l

The performance of the proposed model exhibits a relationship with the number of learnable queries (N_l). In the following, we focus on the general trends and patterns observed in the results.

To better visualize the impact of N_l on the model’s effectiveness, we normalize the results across benchmarks using min-max scaling, ensuring consistency in comparison regardless of differing scales. The normalization is $\mathbf{x} \leftarrow (\mathbf{x} - \min(\mathbf{x})) / (\max(\mathbf{x}) - \min(\mathbf{x}))$, which scales all results to the range $[0, 1]$. This preprocessing step makes it easier to compare performance trends across various benchmarks. The normalized results reveal several distinct trends when plotted. To better understand these patterns, we apply K-means clustering, dividing the results into four clusters. These clusters provide insights into how N_l influences the model’s performance, enabling a more structured analysis of its scaling capability and identifying optimal configurations for various scenarios.

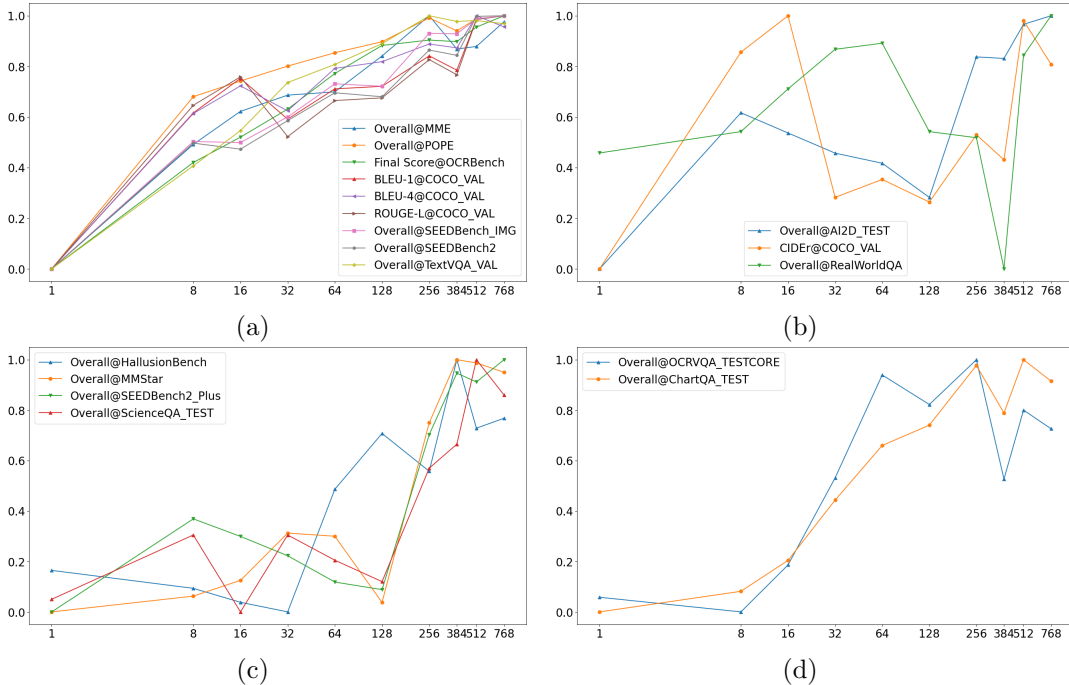


Figure 16: Four clusters illustrating the model’s performance with respect to N_l . The values are normalized using min-max scaling, and the x-axis represents $\log_2(N_l)$. The fused models are taken vision token, user’s question, and learnable queries as inputs.

We begin our analysis with the model that takes vision tokens, the user’s question, and learnable queries as inputs. The results, illustrated in Figure 16, reveal distinct clusters that demonstrate the relationship between the number of learnable queries (N_l) and the model’s performance.

A global observation from the results is that the model performs poorly across all benchmarks when N_l is small. As N_l increases, the performance improves significantly, eventually

stabilizing at higher values of N_l . This indicates that N_l plays a crucial role in enabling the model to achieve strong performance.

Figure 16a shows a nearly proportional relationship between performance and $\log_2(N_l)$, indicating a consistent scaling behavior in this cluster. In Figure 16c, the model exhibits poor performance for $N_l < 128$, followed by a rapid improvement as N_l increases, eventually stabilizing at higher values of N_l . Similarly, in Figure 16d, the model performs poorly for $N_l < 64$, but as N_l grows, the performance increases rapidly and stabilizes. These findings further emphasize the importance of N_l in achieving optimal performance.

Nevertheless, the behavior observed in Figure 16b is less consistent compared to the other clusters. While the performance initially improves as N_l increases within a specific range, it declines beyond that range before recovering again when $N_l \geq 512$. This drop in performance is reminiscent of the trend seen in Figure 16c, where a notable decrease is observed in the range $[8, 128]$, followed by an improvement as $N_l \geq 384$. This behavior suggests that there could be fluctuations within certain ranges of N_l on some tasks or datasets.

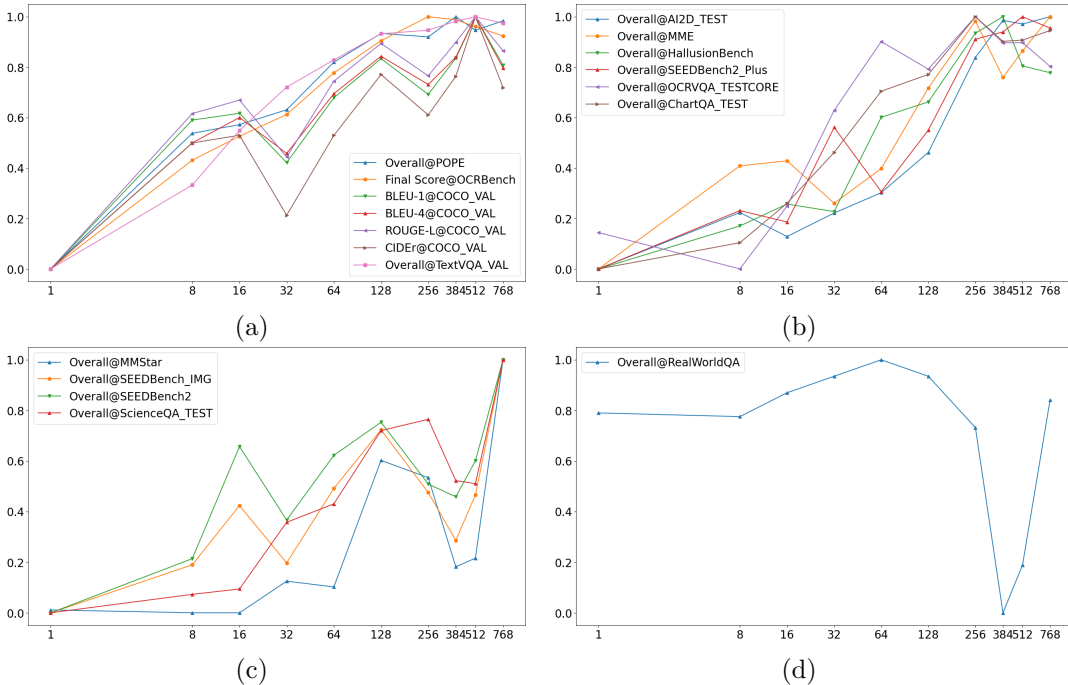


Figure 17: Four clusters illustrating the model’s performance with respect to N_l . The values are normalized using min-max scaling, and the x-axis represents $\log_2(N_l)$. The fused models accept the vision token and learnable queries as inputs, and discard the user’s question.

To explore the impact of incorporating the user’s text question on the model’s performance, we evaluate a configuration where the model excludes the user’s question as input. Instead, the model uses only vision tokens and learnable queries as inputs. For this analysis, we reuse the model described in Appendix C and further fine-tune it under this modified configuration. The performance trends for this setup are illustrated in Figure 17, which presents four clusters revealing interesting patterns with respect to N_l .

Figures 17a and 16d demonstrate similar behavior, with the performance approximately proportional to $\log_2(N_l)$, suggesting a consistent scaling trend. In contrast, Figures 17c and 17d show less clear linear behaviors. In these clusters, the performance initially improves with increasing N_l , then declines within certain ranges, before recovering as N_l becomes sufficiently large. This behavior closely resembles the trends observed in Figure 16c, indicating that intermediate values of N_l may lead to temporary instability or inefficiencies in the model’s performance.

Appendix F. Example of Inference

The following examples illustrate two demonstrations of the generation results produced by the models.



User’s question: “Please describe the image in full detail.”

Model	Generation
$N_l = 1$	The image is of a small river flowing through a green landscape. The river is surrounded by trees and rocks , and there are several bridges crossing it. The river is also lined with rocks and greenery.
$N_l = 8$	The image is of a river flowing through a city. There are trees and buildings along the riverbank. The river is surrounded by a concrete wall. There are also some rocks in the river.
$N_l = 16$	The image is of a river flowing through a concrete channel. The river is surrounded by trees and buildings. There are also some houses and a bridge in the background.
$N_l = 32$	The image shows a long, narrow, concrete drainage ditch running along a wall of a building. The ditch is surrounded by trees and greenery, and there are people walking along the wall. The wall is made of brick and has a large pipe running along it.
$N_l = 64$	The image is of a canal or river with a wall on one side and a building on the other. There are trees and greenery along the wall.
$N_l = 128$	A canal is surrounded by a wall and has a green tree growing on it.
$N_l = 256$	The image is a scenic view of a canal, with a wall on the left and a fence on the right. The canal is surrounded by trees, with leaves and branches visible. There are also houses and buildings visible in the background. The image is quite detailed, with a lot of elements visible.
$N_l = 384$	A canal with a concrete wall and a tree growing on the side.

$N_l = 512$	The image shows a scene of a canal with a wall on the side, surrounded by trees and houses. The canal is filled with water, and there are reflections of the trees and houses on the water. The wall is made of concrete, and there are houses on the other side of the canal.
$N_l = 768$	The image shows a scene of a canal, with a wall of trees on one side and a fence on the other. The canal is surrounded by a concrete wall, and there are trees growing on the wall. The trees are lush and green, with leaves and branches visible. There are also people walking along the fence, adding to the scene's vibrancy.
LLaVA-v1.5-7B-hf	The image features a small stream of water flowing through a city, surrounded by trees and buildings. The stream is lined with trees, creating a serene atmosphere. There are several people scattered throughout the scene, some closer to the water and others further away. In the background, a car can be seen parked near the stream, indicating that the area is accessible to pedestrians and vehicles . The combination of the waterway, trees, and people creates a picturesque urban scene.
InstructBLIP-7B-hf	The image features a narrow canal or river running alongside a building, with trees lining the water's edge. There are several trees visible along the canal, with some closer to the water and others further away. The trees are spread out along the canal, creating a serene and peaceful atmosphere. A few cars can be seen parked along the side of the canal, adding to the urban setting.

- (a) The equation of the graph is $y = 2x - 1$, and we recognize this as being the equation of a line with slope 2 and y-intercept -1 . (Recall the slope-intercept form of the equation of a line: $y = mx + b$. See Appendix B.) This enables us to sketch a portion of the graph of f in Figure 7. The expression $2x - 1$ is defined for all real numbers, so the domain of f is the set of all real numbers, which we denote by \mathbb{R} . The graph shows that the range is also \mathbb{R} .
- (b) Since $g(2) = 2^2 = 4$ and $g(-1) = (-1)^2 = 1$, we could plot the points $(2, 4)$ and $(-1, 1)$, together with a few other points on the graph, and join them to produce the graph (Figure 8). The equation of the graph is $y = x^2$, which represents a parabola (see Appendix C). The domain of g is \mathbb{R} . The range of g consists of all values of $g(x)$, that is, all numbers of the form x^2 . But $x^2 \geq 0$ for all numbers x and any positive number y is a square. So the range of g is $\{y \mid y \geq 0\} = [0, \infty)$. This can also be seen from Figure 8.

User's question: "Please read all text from the image."

Model	Generation
$N_l = 1$	-----
$N_l = 8$	<p>$x^2 = 0$.</p> <p>The equation is a linear equation in two variables, x and y.</p> <p>The graph of the equation is a straight line.</p> <p>The equation is a function of x and y.</p> <p>The equation is a function of</p>

<p>$N_l = 16$</p>	<p>The equation of the line is: $(y=m*x+b)$, where m is the slope of the line and b is the y-intercept. The slope of the line is the ratio of the change in the y-coordinate to the change in the x-coordinate. In other words, it is the rate at which the line rises or falls. The y-intercept is the point at which the line crosses the y-axis. The slope of a line can be calculated by dividing the change in the y-coordinate by the change in the x-coordinate. For example, if the line passes through the point $(2, 3)$, the slope is $3/2$. The y-intercept can be calculated by adding the slope to the point at which the line crosses the y-axis. For example, if the line passes through the point $(2, 3)$, the y-intercept is 3. The equation of a line can be written in the form: $(y=m*x+b)$, where m is the slope and b is the y-intercept. The equation of a line can also be written in the form: $(y=m*x+c)$, where m</p>
<p>$N_l = 32$</p>	<p>## 3.1.1 The equation is: $\begin{aligned}$ $\text{the equation is} \ \&= \ \text{as we are expecting} \ \backslash\backslash$ $\text{and} \ \&= \ \text{the slope of the line is} \ \backslash\backslash$ $\text{the slope of the line is} \ \&= \ \text{the slope of the line is} \ \backslash\backslash$ $\text{the slope of the line is} \ \&= \ \text{the slope of the line is}$</p>
<p>$N_l = 64$</p>	<p>## The equation of a line with slope and y-intercept The equation of a line: $y = mx + b$. + See Appendix B. + See Appendix C. + See Appendix D. The graph of the equation in Figure 7.2 is defined for all values of x. The expression $x = 0$ is defined for all values of y. The range of the graph is also \mathbb{R}. Since $g = 2$ since $g = 1$ and $g = -1$, we can write the equation of the line as: $y = mx + b$. + See Appendix B. + See Appendix C. + See Appendix D. The equation of a line with slope and y-intercept is a linear equation. The slope of the line is m, and the y-intercept is b. The equation of a line with slope and y-intercept is a linear equation. The slope of the line is m, and the y-intercept is b. The equation of a line with slope and y-intercept is a linear</p>
<p>$N_l = 128$</p>	<p>The equation of a line with slope s and a point (x,y) is $2x - y = s$. We recognize this as the equation of a line in slope-intercept form of a line: $mx + b = x$. See Appendix B. This enables us to sketch a portion of the graph of f in Figure 7. The expression 2 is defined for all real numbers, so the domain of f is the set of all real numbers, which we denote by \mathbb{R}. The graph shows that so is also \mathbb{R}. (2) Since $g(2) = s$ since $g(2) = s$, we could plot the points $(2,4)$ and $(1,1)$ on the graph. $(1,-1), 1, 1,$</p>

$N_l = 256$	<p>The equation of the graph is $y = 2x - 1$, and we recognize this as being the equation of a line with slope 2 and y-intercept -1. (Recall the slope-intercept form of the equation of a line: $y = mx + b$. See Appendix B.) This enables us to sketch a portion of the graph of f in Figure 7. The expression $2x - 1$ is defined for all real numbers, so the domain of f is the set of all real numbers, which we denote by \mathbb{R}. The graph shows that the range is also \mathbb{R}.</p> <p>$\left(\begin{array}{c} \text{Since } g(2)=2=1, \text{ we could plot the points } (2,4) \text{ and } (1,1) \text{ together, with a few other points on the graph, and join them to produce the graph (Figure 8). The equation of the graph is } y = x^2, \text{ which represents a parabola (see Appendix C). The domain of } g \text{ is } \mathbb{R}. \text{ The range of } g \text{ consists of all values of } g(x), \text{ that is, all numbers of the form } x^2. \text{ But } x^2 > 0 \text{ for any positive number } y \text{ is a square. So the range of } g \text{ is } [y \mid y \geq 0]. \text{ This can also be seen from Figure 8.}$</p>
$N_l = 384$	<p>(a) The equation of the graph is $y = 2x - 1$, and we recognize this as being the equation of a line with slope 2 and y-intercept 1. (Recall the slope-intercept form of the equation of a line: $y = mx + b$. See Appendix B.) This enables us to sketch a portion of the graph of f in Figure 7. The expression $2x - 1$ is defined for all real numbers, so the domain of f is the set of all real numbers, which we denote by \mathbb{R}. The graph shows that the range is also \mathbb{R}. (b) Since $g(2) = 2a = -1$, we could plot the points $(2, 4)$ and $(1, 1)$, together with a few other points on the graph, and join them to produce the graph (Figure 8). The equation of the graph is $y = x^2$, which represents a parabola (see Appendix C). The domain of g is \mathbb{R}. The range of g consists of all values of $g(x)$, that is, all numbers of the form x^2. But $x^2 > 0$ for all numbers and any positive number y is a. So the range of g is $[0, y] = [0, y] = [0, y] = [0, y] =$</p>
$N_l = 512$	<p>* The equation of the graph is $y = 2x - 1$, and we recognize this as being the equation of a line with slope 2 and y-intercept -1. (Recall the slope-intercept form of the equation of a line: $y = mx + b$. See Appendix B.) This enables us to sketch a portion of the graph of f in Figure 7. The expression $2x - 1$ is defined for all real numbers, so the domain of f is the set of all real numbers, which we denote by \mathbb{R}. The graph shows that the range is also \mathbb{R}. (b) Since $g(2) = 2 = 1$, we could plot the points $(2, 4)$ and $(1, -1)$, together with a few other points on the graph, and join them to produce the graph (Figure 8). The equation of the graph is $y = x^2$, which represents a parabola (see Appendix C). The domain of g is \mathbb{R}. The range of g consists of all numbers of the form x^2. But $x^2 > 0$ for any positive number y is a square. So the range of g is $y = 0 = 0$, or $y = 0 = 0$. This can also be seen from Figure 8.</p>

<p>$N_l = 768$</p>	<pre> <table> <thead> <tr> <td>The equation of the graph is $y = 2x - 1$, and we recognize this as being the equation of a line with slope 2 and y-intercept -1. (Recall the slope-intercept form of the equation of a line: $y = mx + b$. See Appendix B.) This enables us to sketch a portion of the graph of f in Figure 7. The expression $2x - 1$ is defined for all real numbers, so the domain of f is the set of all real numbers, which we denote by \mathbb{R}. The graph shows that the range is also \mathbb{R}. (b) Since $g(2) = 2 = (1 - 1) = (1 - 1)$, together with a few other points on the graph, and join them to produce the graph (Figure 8). The equation of the graph is $y = x^2$, which represents a parabola (see Appendix C). The domain of g is \mathbb{R}. The range of g consists of all values of g, that is, all numbers of the form x^2. But $x^2 > 0$ for any positive number y is a square. So the range of g is $[y \mid y \mid y] = [0 \mid 0 \mid 0]$. This can also be seen from Figure 8. </pre>
<p>LLaVA-v1.5-7B-hf</p>	<p>The image displays a graph with a slope, and the equation is written below it. The graph is described as a "real number" graph, and the slope is defined as a "real number." The equation is written in terms of the slope, and the graph is described as a "real number" graph. The slope is also described as a "real number." The equation is written in terms of the slope, and the graph is described as a "real number" graph. The slope is also described as a</p>
<p>InstructBLIP-7B-hf</p>	<p>the example of graph is shown in the following</p>

References

- M. I. Abdin, S. A. Jacobs, A. A. Awan, J. Aneja, A. Awadallah, H. Awadalla, et al. Phi-3 technical report: A highly capable language model locally on your phone. *CoRR*, abs/2404.14219, 2024. doi: 10.48550/ARXIV.2404.14219. URL <https://doi.org/10.48550/arXiv.2404.14219>.
- J. Alayrac, J. Donahue, P. Luc, A. Miech, I. Barr, Y. Hasson, et al. Flamingo: a visual language model for few-shot learning. In S. Koyejo, S. Mohamed, A. Agarwal, D. Belgrave, K. Cho, and A. Oh, editors, *Annual Conference on Neural Information Processing Systems, NeurIPS, New Orleans, LA, USA, November 28 - December 9, 2022*, 2022. URL http://papers.nips.cc/paper_files/paper/2022/hash/960a172bc7fbf0177ccccbb411a7d800-Abstract-Conference.html.

- Anthropic. The claude 3 model family: Opus, sonnet, haiku. https://www-cdn.anthropic.com/de8ba9b01c9ab7cbabf5c33b80b7bbc618857627/Model_Card_Claude_3.pdf, 2024. Large language model.
- J. Bai, S. Bai, Y. Chu, Z. Cui, K. Dang, X. Deng, et al. Qwen technical report. *CoRR*, abs/2309.16609, 2023a. doi: 10.48550/ARXIV.2309.16609. URL <https://doi.org/10.48550/arXiv.2309.16609>.
- J. Bai, S. Bai, S. Yang, S. Wang, S. Tan, P. Wang, et al. Qwen-vl: A frontier large vision-language model with versatile abilities, 2023b. URL <https://doi.org/10.48550/arXiv.2308.12966>.
- R. Bavishi, E. Elsen, C. Hawthorne, M. Nye, A. Odena, A. Somani, and S. Taşırlar. Introducing our multimodal models, 2023. URL <https://www.adept.ai/blog/fuyu-8b>.
- L. Blecher, G. Cucurull, T. Scialom, and R. Stojnic. Nougat: Neural optical understanding for academic documents. In *International Conference on Learning Representations, ICLR 2024, Vienna, Austria, May 7-11, 2024*. OpenReview.net, 2024. URL <https://openreview.net/forum?id=fUtxNAKpdV>.
- T. B. Brown, B. Mann, N. Ryder, M. Subbiah, J. Kaplan, P. Dhariwal, et al. Language models are few-shot learners. In H. Larochelle, M. Ranzato, R. Hadsell, M. Balcan, and H. Lin, editors, *Annual Conference on Neural Information Processing Systems, NeurIPS, December 6-12, 2020, virtual*, 2020. URL <https://proceedings.neurips.cc/paper/2020/hash/1457c0d6bfc4967418bfb8ac142f64a-Abstract.html>.
- L. Chen, J. Li, X. Dong, P. Zhang, Y. Zang, Z. Chen, et al. Are we on the right way for evaluating large vision-language models? *CoRR*, abs/2403.20330, 2024a. doi: 10.48550/ARXIV.2403.20330. URL <https://doi.org/10.48550/arXiv.2403.20330>.
- Z. Chen, J. Wu, W. Wang, W. Su, G. Chen, S. Xing, et al. Internvl: Scaling up vision foundation models and aligning for generic visual-linguistic tasks. In *Proceedings of the IEEE/CVF Conference on Computer Vision and Pattern Recognition*, pages 24185–24198, 2024b.
- W.-L. Chiang, Z. Li, Z. Lin, Y. Sheng, Z. Wu, H. Zhang, et al. Vicuna: An open-source chatbot impressing gpt-4 with 90% chatgpt quality, March 2023. URL <https://lmsys.org/blog/2023-03-30-vicuna/>.
- W. Dai, J. Li, D. Li, A. M. H. Tiong, J. Zhao, W. Wang, et al. Instructblip: Towards general-purpose vision-language models with instruction tuning. In A. Oh, T. Naumann, A. Globerson, K. Saenko, M. Hardt, and S. Levine, editors, *Annual Conference on Neural Information Processing Systems, NeurIPS, New Orleans, LA, USA, December 10 - 16, 2023*, 2023. URL http://papers.nips.cc/paper_files/paper/2023/hash/9a6a435e75419a836fe47ab6793623e6-Abstract-Conference.html.
- X. Dong, P. Zhang, Y. Zang, Y. Cao, B. Wang, L. Ouyang, et al. Internlm-xcomposer2-4khd: A pioneering large vision-language model handling resolutions from 336 pixels to

- 4k HD. *CoRR*, abs/2404.06512, 2024. doi: 10.48550/ARXIV.2404.06512. URL <https://doi.org/10.48550/arXiv.2404.06512>.
- H. Duan, J. Yang, Y. Qiao, X. Fang, L. Chen, Y. Liu, et al. Vlmevalkit: An open-source toolkit for evaluating large multi-modality models. In J. Cai, M. S. Kankanhalli, B. Prabhakaran, S. Boll, R. Subramanian, L. Zheng, V. K. Singh, P. César, L. Xie, and D. Xu, editors, *ACM International Conference on Multimedia, MM 2024, Melbourne, VIC, Australia, 28 October 2024 - 1 November 2024*, pages 11198–11201. ACM, 2024. doi: 10.1145/3664647.3685520. URL <https://doi.org/10.1145/3664647.3685520>.
- A. Dubey, A. Jauhri, A. Pandey, A. Kadian, A. Al-Dahle, et al. The llama 3 herd of models. *CoRR*, abs/2407.21783, 2024. doi: 10.48550/ARXIV.2407.21783. URL <https://doi.org/10.48550/arXiv.2407.21783>.
- C. Fu, P. Chen, Y. Shen, Y. Qin, M. Zhang, X. Lin, et al. MME: A comprehensive evaluation benchmark for multimodal large language models. *CoRR*, abs/2306.13394, 2023. doi: 10.48550/ARXIV.2306.13394. URL <https://doi.org/10.48550/arXiv.2306.13394>.
- S. Ghosh, S. Kumar, A. Seth, C. K. R. Evuru, U. Tyagi, et al. GAMA: A large audio-language model with advanced audio understanding and complex reasoning abilities. In Y. Al-Onaizan, M. Bansal, and Y. Chen, editors, *Empirical Methods in Natural Language Processing, EMNLP, Miami, FL, USA, November 12-16, 2024*, pages 6288–6313. Association for Computational Linguistics, 2024. URL <https://aclanthology.org/2024.emnlp-main.361>.
- Y. Gong, H. Luo, A. H. Liu, L. Karlinsky, and J. R. Glass. Listen, think, and understand. In *International Conference on Learning Representations, ICLR, Vienna, Austria, May 7-11, 2024*. OpenReview.net, 2024. URL <https://openreview.net/forum?id=nBZBPXdJ1C>.
- T. Guan, F. Liu, X. Wu, R. Xian, Z. Li, X. Liu, et al. Hallusionbench: An advanced diagnostic suite for entangled language hallucination and visual illusion in large vision-language models. In *IEEE/CVF Conference on Computer Vision and Pattern Recognition, CVPR, Seattle, WA, USA, June 16-22, 2024*, pages 14375–14385. IEEE, 2024. doi: 10.1109/CVPR52733.2024.01363. URL <https://doi.org/10.1109/CVPR52733.2024.01363>.
- W. Hong, W. Wang, M. Ding, W. Yu, Q. Lv, Y. Wang, et al. Cogvlm2: Visual language models for image and video understanding. *CoRR*, abs/2408.16500, 2024. doi: 10.48550/ARXIV.2408.16500. URL <https://doi.org/10.48550/arXiv.2408.16500>.
- A. Hu, H. Xu, J. Ye, M. Yan, L. Zhang, B. Zhang, et al. mplug-docowl 1.5: Unified structure learning for ocr-free document understanding. In Y. Al-Onaizan, M. Bansal, and Y. Chen, editors, *Findings of the Association for Computational Linguistics: EMNLP, Miami, Florida, USA, November 12-16, 2024*, pages 3096–3120. Association for Computational Linguistics, 2024. URL <https://aclanthology.org/2024.findings-emnlp.175>.
- J. Kaplan, S. McCandlish, T. Henighan, T. B. Brown, B. Chess, et al. Scaling laws for neural language models. *CoRR*, abs/2001.08361, 2020. URL <https://arxiv.org/abs/2001.08361>.

- H. Laurençon, L. Tronchon, M. Cord, and V. Sanh. What matters when building vision-language models? *CoRR*, abs/2405.02246, 2024. doi: 10.48550/ARXIV.2405.02246. URL <https://doi.org/10.48550/arXiv.2405.02246>.
- B. Li, Y. Ge, Y. Ge, G. Wang, R. Wang, R. Zhang, and Y. Shan. Seed-bench-2: Benchmarking multimodal large language models. *CoRR*, abs/2311.17092, 2023a. doi: 10.48550/ARXIV.2311.17092. URL <https://doi.org/10.48550/arXiv.2311.17092>.
- B. Li, Y. Ge, Y. Chen, Y. Ge, R. Zhang, and Y. Shan. Seed-bench-2-plus: Benchmarking multimodal large language models with text-rich visual comprehension. *CoRR*, abs/2404.16790, 2024a. doi: 10.48550/ARXIV.2404.16790. URL <https://doi.org/10.48550/arXiv.2404.16790>.
- B. Li, Y. Ge, Y. Ge, G. Wang, R. Wang, R. Zhang, and Y. Shan. Seed-bench: Benchmarking multimodal large language models. In *IEEE/CVF Conference on Computer Vision and Pattern Recognition, CVPR 2024, Seattle, WA, USA, June 16-22, 2024*, pages 13299–13308. IEEE, 2024b. doi: 10.1109/CVPR52733.2024.01263. URL <https://doi.org/10.1109/CVPR52733.2024.01263>.
- J. Li, D. Li, C. Xiong, and S. C. H. Hoi. BLIP: bootstrapping language-image pre-training for unified vision-language understanding and generation. In K. Chaudhuri, S. Jegelka, L. Song, C. Szepesvári, G. Niu, and S. Sabato, editors, *International Conference on Machine Learning, ICML, 17-23 July 2022, Baltimore, Maryland, USA*, volume 162 of *Proceedings of Machine Learning Research*, pages 12888–12900. PMLR, 2022. URL <https://proceedings.mlr.press/v162/li22n.html>.
- J. Li, D. Li, S. Savarese, and S. C. H. Hoi. BLIP-2: bootstrapping language-image pre-training with frozen image encoders and large language models. In A. Krause, E. Brunskill, K. Cho, B. Engelhardt, S. Sabato, and J. Scarlett, editors, *International Conference on Machine Learning, ICML, 23-29 July 2023, Honolulu, Hawaii, USA*, volume 202 of *Proceedings of Machine Learning Research*, pages 19730–19742. PMLR, 2023b. URL <https://proceedings.mlr.press/v202/li23q.html>.
- Y. Li, Y. Du, K. Zhou, J. Wang, W. X. Zhao, and J. Wen. Evaluating object hallucination in large vision-language models. In H. Bouamor, J. Pino, and K. Bali, editors, *Empirical Methods in Natural Language Processing, EMNLP 2023, Singapore, December 6-10, 2023*, pages 292–305. Association for Computational Linguistics, 2023c. doi: 10.18653/V1/2023.EMNLP-MAIN.20. URL <https://doi.org/10.18653/v1/2023.emnlp-main.20>.
- T. Lin, M. Maire, S. J. Belongie, J. Hays, P. Perona, D. Ramanan, et al. Microsoft COCO: common objects in context. In D. J. Fleet, T. Pajdla, B. Schiele, and T. Tuytelaars, editors, *Computer Vision - ECCV 2014 - 13th European Conference, Zurich, Switzerland, September 6-12, 2014*, volume 8693 of *Lecture Notes in Computer Science*, pages 740–755. Springer, 2014. doi: 10.1007/978-3-319-10602-1_48. URL https://doi.org/10.1007/978-3-319-10602-1_48.
- H. Liu, C. Li, Q. Wu, and Y. J. Lee. Visual instruction tuning. In A. Oh, T. Naumann, A. Globerson, K. Saenko, M. Hardt, and S. Levine, editors, *Annual Conference*

- on *Neural Information Processing Systems, NeurIPS, New Orleans, LA, USA, December 10 - 16, 2023*, 2023a. URL http://papers.nips.cc/paper_files/paper/2023/hash/6dcf277ea32ce3288914faf369fe6de0-Abstract-Conference.html.
- T. J. B. Liu, N. Boullé, R. Sarfati, and C. J. Earls. Llms learn governing principles of dynamical systems, revealing an in-context neural scaling law. *CoRR*, abs/2402.00795, 2024. doi: 10.48550/ARXIV.2402.00795. URL <https://doi.org/10.48550/arXiv.2402.00795>.
- Y. Liu, Z. Li, H. Li, W. Yu, M. Huang, D. Peng, et al. On the hidden mystery of OCR in large multimodal models. *CoRR*, abs/2305.07895, 2023b. doi: 10.48550/ARXIV.2305.07895. URL <https://doi.org/10.48550/arXiv.2305.07895>.
- H. Lu, W. Liu, B. Zhang, B. Wang, K. Dong, B. Liu, et al. Deepseek-vl: Towards real-world vision-language understanding. *CoRR*, abs/2403.05525, 2024. doi: 10.48550/ARXIV.2403.05525. URL <https://doi.org/10.48550/arXiv.2403.05525>.
- P. Lu, S. Mishra, T. Xia, L. Qiu, K. Chang, S. Zhu, et al. Learn to explain: Multimodal reasoning via thought chains for science question answering. In S. Koyejo, S. Mohamed, A. Agarwal, D. Belgrave, K. Cho, and A. Oh, editors, *Annual Conference on Neural Information Processing Systems, NeurIPS, New Orleans, LA, USA, November 28 - December 9, 2022*, 2022. URL http://papers.nips.cc/paper_files/paper/2022/hash/11332b6b6cf4485b84afadb1352d3a9a-Abstract-Conference.html.
- A. Masry, D. Long, J. Q. Tan, S. Joty, and E. Hoque. ChartQA: A benchmark for question answering about charts with visual and logical reasoning. In *Findings of the Association for Computational Linguistics: ACL 2022*, pages 2263–2279, Dublin, Ireland, May 2022. Association for Computational Linguistics. doi: 10.18653/v1/2022.findings-acl.177. URL <https://aclanthology.org/2022.findings-acl.177>.
- A. Mishra, S. Shekhar, A. K. Singh, and A. Chakraborty. OCR-VQA: visual question answering by reading text in images. In *International Conference on Document Analysis and Recognition, ICDAR 2019, Sydney, Australia, September 20-25, 2019*, pages 947–952. IEEE, 2019. doi: 10.1109/ICDAR.2019.00156. URL <https://doi.org/10.1109/ICDAR.2019.00156>.
- OpenAI. GPT-4 technical report. *CoRR*, abs/2303.08774, 2023. doi: 10.48550/ARXIV.2303.08774. URL <https://doi.org/10.48550/arXiv.2303.08774>.
- A. Radford, J. W. Kim, C. Hallacy, A. Ramesh, G. Goh, and Sandothers. Learning transferable visual models from natural language supervision. In M. Meila and T. Zhang, editors, *International Conference on Machine Learning, ICML, 18-24 July 2021, Virtual Event*, volume 139 of *Proceedings of Machine Learning Research*, pages 8748–8763. PMLR, 2021. URL <http://proceedings.mlr.press/v139/radford21a.html>.
- R. Rafailov, A. Sharma, E. Mitchell, C. D. Manning, S. Ermon, and C. Finn. Direct preference optimization: Your language model is secretly a reward model. In A. Oh, T. Nauermann, A. Globerson, K. Saenko, M. Hardt, and S. Levine, editors, *Annual Conference on Neural Information Processing Systems, NeurIPS, New Orleans, LA, USA, December*

- 10 - 16, 2023, 2023. URL http://papers.nips.cc/paper_files/paper/2023/hash/a85b405ed65c6477a4fe8302b5e06ce7-Abstract-Conference.html.
- N. Reimers and I. Gurevych. Sentence-bert: Sentence embeddings using siamese bert-networks. In K. Inui, J. Jiang, V. Ng, and X. Wan, editors, *Empirical Methods in Natural Language Processing and the 9th International Joint Conference on Natural Language Processing, EMNLP-IJCNLP 2019, Hong Kong, China, November 3-7, 2019*, pages 3980–3990. Association for Computational Linguistics, 2019. doi: 10.18653/V1/D19-1410. URL <https://doi.org/10.18653/v1/D19-1410>.
- A. Singh, V. Natarajan, M. Shah, Y. Jiang, X. Chen, D. Batra, et al. Towards VQA models that can read. In *IEEE Conference on Computer Vision and Pattern Recognition, CVPR, Long Beach, CA, USA, June 16-20, 2019*, pages 8317–8326. Computer Vision Foundation / IEEE, 2019. doi: 10.1109/CVPR.2019.00851. URL http://openaccess.thecvf.com/content_CVPR_2019/html/Singh_Towards_VQA_Models_That_Can_Read_CVPR_2019_paper.html.
- R. Taori, I. Gulrajani, T. Zhang, Y. Dubois, X. Li, C. Guestrin, et al. Stanford alpaca: An instruction-following llama model. https://github.com/tatsu-lab/stanford_alpaca, 2023.
- H. Touvron, T. Lavril, G. Izacard, X. Martinet, M. Lachaux, T. Lacroix, et al. Llama: Open and efficient foundation language models. *CoRR*, abs/2302.13971, 2023a. doi: 10.48550/ARXIV.2302.13971. URL <https://doi.org/10.48550/arXiv.2302.13971>.
- H. Touvron, L. Martin, K. Stone, P. Albert, A. Almahairi, Y. Babaei, et al. Llama 2: Open foundation and fine-tuned chat models. *CoRR*, abs/2307.09288, 2023b. doi: 10.48550/ARXIV.2307.09288. URL <https://doi.org/10.48550/arXiv.2307.09288>.
- W. Wang, Q. Lv, W. Yu, W. Hong, J. Qi, Y. Wang, et al. Cogvlm: Visual expert for pretrained language models. *CoRR*, abs/2311.03079, 2023. doi: 10.48550/ARXIV.2311.03079. URL <https://doi.org/10.48550/arXiv.2311.03079>.
- J. Ye, A. Hu, H. Xu, Q. Ye, M. Yan, Y. Dan, et al. mplug-docowl: Modularized multimodal large language model for document understanding. *CoRR*, abs/2307.02499, 2023a. doi: 10.48550/ARXIV.2307.02499. URL <https://doi.org/10.48550/arXiv.2307.02499>.
- Q. Ye, H. Xu, J. Ye, M. Yan, A. Hu, H. Liu, et al. mplug-owl2: Revolutionizing multi-modal large language model with modality collaboration. volume abs/2311.04257, 2023b. doi: 10.48550/ARXIV.2311.04257. URL <https://doi.org/10.48550/arXiv.2311.04257>.
- A. Zeng, B. Xu, B. Wang, C. Zhang, D. Yin, D. Rojas, et al. Chatglm: A family of large language models from GLM-130B to GLM-4 all tools. *CoRR*, abs/2406.12793, 2024. doi: 10.48550/ARXIV.2406.12793. URL <https://doi.org/10.48550/arXiv.2406.12793>.
- X. Zhai, B. Mustafa, A. Kolesnikov, and L. Beyer. Sigmoid loss for language image pre-training. In *IEEE/CVF International Conference on Computer Vision, ICCV, Paris, France, October 1-6, 2023*, pages 11941–11952. IEEE, 2023. doi: 10.1109/ICCV51070.2023.01100. URL <https://doi.org/10.1109/ICCV51070.2023.01100>.

- H. Zhang, X. Li, and L. Bing. Video-llama: An instruction-tuned audio-visual language model for video understanding. In Y. Feng and E. Lefever, editors, *Empirical Methods in Natural Language Processing, EMNLP System Demonstrations, Singapore, December 6-10, 2023*, pages 543–553. Association for Computational Linguistics, 2023. doi: 10.18653/V1/2023.EMNLP-DEMO.49. URL <https://doi.org/10.18653/v1/2023.emnlp-demo.49>.
- B. Zhao, B. Wu, and T. Huang. SVIT: scaling up visual instruction tuning. *CoRR*, abs/2307.04087, 2023. doi: 10.48550/ARXIV.2307.04087. URL <https://doi.org/10.48550/arXiv.2307.04087>.
- D. Zhu, J. Chen, X. Shen, X. Li, and M. Elhoseiny. Minigt-4: Enhancing vision-language understanding with advanced large language models. In *International Conference on Learning Representations, ICLR, Vienna, Austria, May 7-11, 2024*. OpenReview.net, 2024. URL <https://openreview.net/forum?id=1tZbq88f27>.